NAVAL POSTGRADUATE SCHOOL

MONTEREY, CALIFORNIA

THESIS

DETECTION OF SPATIALLY UNRESOLVED (NOMINALLY SUB-PIXEL) SUBMERGED AND SURFACE TARGETS USING HYPERSPECTRAL DATA

by

Christopher Burt

September 2012

Thesis Advisor:	Richard C. Olsen
Second Reader:	David Trask

Approved for public release, distribution is unlimited

THIS PAGE INTENTIONALLY LEFT BLANK

REPORT DOCUMENTATION PAGE		*Form Approved OMB No. 0704-0188*

Public reporting burden for this collection of information is estimated to average 1 hour per response, including the time for reviewing instruction, searching existing data sources, gathering and maintaining the data needed, and completing and reviewing the collection of information. Send comments regarding this burden estimate or any other aspect of this collection of information, including suggestions for reducing this burden, to Washington headquarters Services, Directorate for Information Operations and Reports, 1215 Jefferson Davis Highway, Suite 1204, Arlington, VA 22202-4302, and to the Office of Management and Budget, Paperwork Reduction Project (0704-0188) Washington DC 20503.

1. AGENCY USE ONLY *(Leave blank)*	2. REPORT DATE September 2012	3. REPORT TYPE AND DATES COVERED Master's Thesis
4. TITLE AND SUBTITLE Detection of Spatially Unresolved (Nominally Sub-Pixel) Submerged and Surface Targets Using Hyperspectral Data		5. FUNDING NUMBERS
6. AUTHOR(S) Christopher B. Burt		

7. PERFORMING ORGANIZATION NAME(S) AND ADDRESS(ES)
    Naval Postgraduate School
    Monterey, CA 93943-5000
		8. PERFORMING ORGANIZATION REPORT NUMBER

9. SPONSORING /MONITORING AGENCY NAME(S) AND ADDRESS(ES) Remote Sensing Center, Naval Postgraduate School		10. SPONSORING/MONITORING AGENCY REPORT NUMBER

11. SUPPLEMENTARY NOTES The views expressed in this thesis are those of the author and do not reflect the official policy or position of the Department of Defense or the U.S. Government. IRB Protocol number _____.

12a. DISTRIBUTION / AVAILABILITY STATEMENT Approved for public release, distribution is unlimited	12b. DISTRIBUTION CODE A

13. ABSTRACT (maximum 200 words)

Due to the United States' dependency on maritime travel, the proliferation of efficient and inexpensive naval mines poses a tremendous risk. Current MCM technologies have narrow FOVs, preventing timely, wide-area searches. These technologies require the operator to be in proximity to the targets, a dangerous scenario made worse when in denied territory.

In an effort to mitigate these risks, the use of a high altitude hyperspectral sensor is proposed. The operational ability of a hyperspectral sensor to detect sub-pixel surface and submerged mines in non-littoral environments was evaluated using visual inspection and two common anomaly detectors: Mixture Tuned Matched Filtering (MTMF) and Reed-Xiaoli (RX). Due to the unavailability of the DoD's Spectral Infrared Imaging Technology Testbed (SPIRITT), ProSpecTIR-VS3, a sensor similar spatially and spectrally to SPIRITT was flown over a range offshore California. This experiment included three surface and three submerged targets, each with a 0.8 meter diameter. Both 0.5 and 1 meter spatial resolution data were collected, allowing for both a resolved and unresolved analysis.

While both anomaly detection techniques have their flaws, the success of this study is in proving the usefulness of hyperspectral data for sub-pixel mine detection.

14. SUBJECT TERMS Type Keywords Here	15. NUMBER OF PAGES 115
	16. PRICE CODE

17. SECURITY CLASSIFICATION OF REPORT SECRET	18. SECURITY CLASSIFICATION OF THIS PAGE Unclassified	19. SECURITY CLASSIFICATION OF ABSTRACT Unclassified	20. LIMITATION OF ABSTRACT UL

NSN 7540-01-280-5500

Standard Form 298 (Rev. 2-89)
Prescribed by ANSI Std. 239-18

THIS PAGE INTENTIONALLY LEFT BLANK

DETECTION OF SPATIALLY UNRESOLVED (NOMINALLY SUB-PIXEL) SUBMERGED AND SURFACE TARGETS USING HYPERSPECTRAL DATA

Christopher B. Burt
Civilian, Department of Defense
B.S., University of California, Santa Barbara, 2007

Submitted in partial fulfillment of the
requirements for the degree of

MASTER OF SCIENCE IN REMOTE SENSING INTELLIGENCE

from the

**NAVAL POSTGRADUATE SCHOOL
September 2012**

Author: Christopher B. Burt

Approved by: Richard C. Olsen
                 Thesis Advisor

                 David Trask
                 Second Reader

                 Dan Boger
                 Chair, Department of Information Sciences

iii

THIS PAGE INTENTIONALLY LEFT BLANK

ABSTRACT

Due to the United States' dependency on maritime travel, the proliferation of efficient and inexpensive naval mines poses a tremendous risk. Current MCM technologies have narrow FOVs, preventing timely, wide-area searches. These technologies require the operator to be in proximity to the targets, a dangerous scenario made worse when in denied territory.

In an effort to mitigate these risks, the use of a high altitude hyperspectral sensor is proposed. The operational ability of a hyperspectral sensor to detect sub-pixel surface and submerged mines in non-littoral environments was evaluated using visual inspection and two common anomaly detectors: Mixture Tuned Matched Filtering (MTMF) and Reed-Xiaoli (RX). Due to the unavailability of the DoD's Spectral Infrared Imaging Technology Testbed (SPIRITT), ProSpecTIR-VS3, a sensor similar spatially and spectrally to SPIRITT was flown over a range offshore California. This experiment included three surface and three submerged targets, each with a 0.8 meter diameter. Both 0.5 and 1 meter spatial resolution data were collected, allowing for both a resolved and unresolved analysis.

While both anomaly detection techniques have their flaws, the success of this study is in proving the usefulness of hyperspectral data for sub-pixel mine detection.

THIS PAGE INTENTIONALLY LEFT BLANK

TABLE OF CONTENTS

LIST OF FIGURES

v

LIST OF TABLES

THIS PAGE INTENTIONALLY LEFT BLANK

LIST OF ACRONYMS AND ABBREVIATIONS

ACES-HY   Airborne Cueing and Exploitation System, Hyperspectral

ALMDS   Airborne Laser Mine Detection System

AUV   Automated Underwater Vehicle

AVIRIS   Airborne Visible/Infrared Imaging Spectrometer

BRDF   Bidirectional Reflectance Distribution Function

CASI   Compact Airborne Spectrographic Imager

CCD   Charge-Coupled Device

COBRA   Coastal Battlefield Reconnaissance and Analysis

DN   Digital Number

FN   False Negative

FP   False Positive

FPR   False Positive Rate

FWHM   Full Width at Half Maximum

GIS   Geographic Information System

GLT   Geographic Lookup Table

GMRF   Gauss-Markov Random Field

GPS   Global Positioning System

GSD   Ground Sample Distance

HSI   Hyperspectral Imagery

IGM   Internal Geometry Map

IMU   Inertial Measurement Unit

INS   Inertial Navigation System

IR   Infrared

ISM	Invariant Subspace Method
ISR	Intelligence, Surveillance, and Reconnaissance
JPL	Jet Propulsion Laboratory
LASH	Littoral Airborne Sensor, Hyperspectral
LiDAR	Light Detection and Ranging
LMW	Littoral and Mine Warfare
LPD	Low Probability Detector
MCM	Mine Countermeasures
MF	Matched Filter
mine	Naval Sea Mine
MNF	Minimum Noise Fraction
MODTRAN	Moderate resolution atmospheric Transmission
MTMF	Mixture Tuned Matched Filtering
nm	Nanometer (10^{-9} meters)
PC	Principle Component
PCA	Principle Component Analysis
PEO	Program Executive Office
PPI	Pixel Purity Index
REMUS	Remote Environmental Measuring Unit
RMMV	Remote Multi-Mission Vehicle
ROC	Receiver Operating Characteristics
ROI	Region of Interest
ROV	Remotely Operated Vehicle
RX	Reed-Xiaoli
RXD	Reed-Xiaoli Detector

SAR	Synthetic Aperture Radar
SPIRITT	Spectral Infrared Remote Imaging Transit Testbed
SVDD	Support Vector Data Description
SWIR	Short-Wave Infrared
TACMSI	Tactical Multispectral Imager
TN	True Negative
TN	True Negative
TP	True Positive
TPR	True Positive Rate
U.N.	United Nations
U.S.	United States
UAV	Unmanned Aerial Vehicle
USAF	United States Air Force
USN	United States Navy
UTD	Uniform Target Detector
VNIR	Visible and Near Infrared

THIS PAGE INTENTIONALLY LEFT BLANK

ACKNOWLEDGMENTS

THIS PAGE INTENTIONALLY LEFT BLANK

I. INTRODUCTION

. . . when you can't go where you want to when you want to, you haven't
got command of the sea. And command of the sea is a rock-bottom
foundation for all our war plans. – Admiral Forrest Sherman, 1950
(Program Executive Office Littoral and Mine Warfare, 2009, p.5)

Due to the United States' dependency on both international and domestic maritime travel, the proliferation of efficient and inexpensive naval mines poses a tremendous risk. More than 50 nations have the ability to effectively shut down waterways with naval mines. These weapons are easy to produce and according to recent published reports, global stockpiles are surging. Many recent national directives, including the U.S. National Strategy for Maritime Security, National Strategy for Homeland Security and National Infrastructure Protection Plan call for the improved ability to detect and neutralize threats to the maritime community, particularly sea mines.

Current United States Mine Countermeasure (MCM) detection tactics require the use of side scan sonar, multibeam bathymetry or airborne light detection and ranging technologies. These sensors, although effective and accurate, have key operational limitations: they require the collection platform to be in close proximity to the targets and have narrow field of views, preventing timely, wide-area surveys. Under even the most ideal scenario, having vessels in the water near mines or aircraft operating at low altitudes creates an extreme risk to the vessel and the operator. In a more realistic scenario, the target mines will be within a denied territory. This would increase the risk to both an airborne and water-based asset. Recent developments in high altitude spectral imaging may allow for timely, wide-area surveys to detect mines in denied territories.

Using data collected by a variety of multispectral and hyperspectral imagers, Winter (2008) explored the feasibility of using a Reed-Xiaoli anomaly detection algorithm and a signature-based pixel unmixing algorithm to locate both sub-pixel and fully resolved mines in a variety of land-based backgrounds. The data for this test were collected at high and low resolutions in order to analyze spatially unresolved and resolved targets. Both of the detection techniques worked flawlessly on the high

1

resolution data as the mines were spatially resolved. The tests had no false negative and no false positives. For the low resolution data, with sub-pixel, spatially unresolved targets, Winter (2008) used the Invariant Subspace Method (ISM) algorithm. This technique is similar to mixture tuned matched filtering (MTMF), and was designed by Healey and Slater (1999) to use "a physical model to generate the set of sensor spectra for a target that will be measured over a range of conditions" (Winter, 2008, p.69530R-6). The results of this test, while not as robust as the spatially resolved test, were encouraging. The ISM algorithm was able to detect 50% of the mines, with no false positives (Winter, 2008). A similar analysis will be done later in this report, using an RX anomaly detector and MTMF analysis technique.

The purpose of this paper is to determine the operational ability of an airborne hyperspectral sensor, spatially and spectrally similar to current Department of Defense sensors, including the Spectral Infrared Imaging Technology Testbed (SPIRITT), to quickly and accurately detect spatially unresolved, sub-pixel mines. The specific targets in this experiment were both surface and submerged (up to 3 meters) mines in deep water (i.e. non-littoral) conditions. In an effort to detect them quickly, a basic anomaly detection wizard was run using ENVI, a common image processing software. Two common hyperspectral detection algorithms were evaluated: the Mixture Tuned Match Filter and the Reed-Xiaoli anomaly detector. The results of Sandersfeld (2012), done concurrent to this study using multispectral WorldView-2 data of the target range, were compared to the results of this paper.

Chapter II of this paper will discuss the background elements to this study, with a brief history of mine warfare. This will give the reader an understanding of the extreme risk posed by mines and why detecting them should a priority. Chapter II will then describe the physics of hyperspectral imaging as well as give a brief overview of common anomaly detection algorithms. Chapter III will give a detailed description of the data collection process and the arranged test. Chapter IV will discuss how the data was processed, while Chapter V will show the results. Finally, Chapter VI will provide conclusions to the study and suggest further research to be done in this field.

II. BACKGROUND

A. SEA MINES

1. History

The origins of sea mine warfare have been linked to the "Greek Fire" used by the Byzantine fleet in 673 AD (PEO LMW, 2009) and the earliest published description of the modern sea mine dates back to the 14th century and the Ming Dynasty. In the military treatise Huolongjing, famous for its early description of gunpowder weapons, Chinese military officers Jiao Yu and Liu Ji first described the concept of the naval sea mine (mine) (Needham & Wang, 1954). Over 400 years after first appearing in printed work, the mine became a practical weapon in 1776. During the American Revolutionary War, David Bushnell, an American inventor known for developing the first combat submarine, created a mine by sealing a wooden keg full of gunpowder and floating it down the Delaware River towards British Warships. These mines had a negligible impact during the American Revolution, but as developments continued, the mine became an effective weapon during the wars since (PEO LMW, 2009).

Modern naval mines were developed by Immanuel Nobel for Russia's use in the Crimean War (1853–1856). His expertise using nitroglycerin and gunpowder made mines reliable and devastating weapons that denied British naval ships access to the strategic Gulf of Finland (Brown, 1990).

Initially written off as an "un-chivalrous" form of warfare, naval mining started to become more common during the American Civil War (1861–1865) (Gilbert, 2001). In a statement regarding the Confederacy's growing use of mines, Rear Admiral David Farragut of the United States Navy (USN) wrote, "I have always deemed it unworthy of a chivalrous nation, but it does not do to give your enemy such a decided superiority over you" (PEO LMW, 2009, p. 3). Confederate mines destroyed 59 ships during the war, including 11 of their own (PEO LMW, 2009).

Mines impacted the Spanish-American War (1898), the Russo-Japanese War (1904–1905), both of the World Wars (1914–1918 and 1939–1945), the Korean War (1950–1953), the Vietnam War (1955–1975), the Iran-Iraq War (1980–1988) and the Gulf War (1990–1991). During World War II, German U-boats placed mines along the United States and Canadian coasts, causing the closure of many ports. As part of Operation Starvation in 1945, the U.S. mined Japanese waters, destroying almost 800 Japanese vessels and shutting down nearly all Japanese maritime commerce. Post-World War II, four times as many USN vessels were damaged or sunk by mines than any other attack. This started during the Korean War when 14 vessels were severely damaged or destroyed by mines, accounting for 78% of the damaged vessels and over 20% of Navy causalities during the conflict. In order to deny access to North Vietnam ports, the United States laid thousands of mines during the Vietnam War, stopping all maritime trade. During the Iran-Iraq War and Gulf War, the belligerents heavily mined the Arabian Gulf and the Strait of Hormuz, causing damage to numerous vessels, including 3 USN ships (PEO LMW, 2009).

In the 5 years between the end of the Gulf War in 1991 and a report published by the United States Senate Armed Services Committee on Expeditionary Warfare in 1996, the number of mines stockpiled globally had increased by over 50%. Currently, global inventories include over 250,000 mines with more than 50 nations having the ability to mine waterways. At least 30 nations are producing 300 different types of mines and more than 20 nations are exporting mines (PEO LMW, 2009).

2.   **Tactical Advantages**

a.   *Cost Effectiveness*

Sea mines are a cost-effective form of warfare, achieving excellent results via an asymmetric warfare campaign. They are easy to place from aircraft, small boats, large ships, divers or even trucks. Compared to the amount of damage they can do to a vessel, mines are not expensive to manufacture or purchase. The SADAF-02 Russian-made and Iranian placed mine that struck the USS Samuel B. Roberts during the Iran-Iraq

War in 1980 cost approximately $1,000, but was able to inflict over $96 million in damage (PEO LMW, 2009). Similarly, during the 1991 Gulf War, the Iraqi-made LUGM-145 and Italian-made Manta mines that damaged the USS Tripoli and USS Princeton collectively cost less than $25,000 to manufacture, but inflicted over $20 million in damage to the vessels (Rios, 2005).

b. Denial of Access

The effectiveness of mines has never been limited to just their ability to damage and / or sink vessels, but their ability to effectively control bodies of water by limiting or slowing naval movements (Truver, 2011). This is particularly effective in narrow bodies of water such as bays and harbors. Twice since the end of World War II the presence of enemy mines has prevented United States military operations. In 1950, during the Korean War, North Korean mines delayed the landing of U.S. and United Nations (U.N.) forces in Wonsan bay for almost a month, allowing enemy soldiers to escape. The frustrated commander of the task force, Rear Admiral Allen E. Smith would later summarize the tactical advantage of mining, bemoaning that, "[U.N. forces had] lost control of the seas to a nation without a navy, using pre-World War I weapons, laid by vessels that were utilized at the time of the birth of Christ" (PEO LMW, 2009, pp. 4–5). After two USN vessels were damaged by mines during the Gulf War in 1991, plans for an amphibious assault on Kuwait City were cancelled for fear of Iraqi mines (PEO LMW, 2009).

c. Psychological Effects

Just the threat of deployed mines is psychologically powerful enough to deny enemy combatants access to a body of water. In fact, "about 90% of all mine hunting and sweeping operations have been conducted in areas in which mines have not been deployed" (PEO LMW, 2009, p. 22). In response to the Soviet grain embargo in January of 1980 an unknown person claimed to have laid a mine in the Sacramento River, an important shipping waterway in Northern California. The threat caused the complete closure of the river for four days as a navy mine-sweeping team searched the river. No

mine was ever found and the threat was deemed a hoax, but the cost to maritime shipping was estimated to be hundreds of thousands of dollars (PEO LMW, 2009).

3. Types of Mines

Mines can be created in a variety of forms, but are traditionally divided into a few different categories, including bottom mines, limpet mines, drifting mines and moored mines. Each mine type is designed for use in certain locations. Moored mines, for instance, are designed to float and are moored to the seafloor. These mines are used mostly in littoral zones and shallow water. Bottom mines are placed on the seafloor and are thus used primarily in littoral zones and at shallow depths. These mines are also placed in deeper water in order to target submarines. Limpet mines are placed directly on the hull of the target vessel and rigged with a detonator. These mines can be used in any water depth, but require a diver to place them. Drifting mines are buoyant and float at, or just below the surface. These mines are found at any water depth and are especially dangerous as they are intended to drift with the current. As such, their exact location and course cannot be determined or controlled. Although the use of drifting mines violates the International Hague Convention of 1907, they are still commonly used by countries such as Iran and Iraq (Rios, 2005).

Each of these mine types have various trigger mechanisms, including chemical horns that trigger on contact, command mines, which can be detonated by remote control and influence mines which trigger based off of built in sensors. Influence mines may use seismic, acoustic, pressure or magnetic sensors to determine when a target is within range (PEO LMW, 2009). The development of computers and sensors has allowed mine triggering mechanisms to become more sophisticated.

4. Mine Countermeasures: Detection

Although mine countermeasure (MCM) doctrine consists of detection, classification and neutralization (Potter, 1999), this research focuses on the detection aspect of MCM.

6

a.   *Brief History*

The first recorded use of mine detection and minesweeping tactics occurred one hundred years after David Bushnell invented the practical mine. During the American Civil War, mine sweeping rafts were created by Union forces. These rafts were made of wood and constructed with grappling hooks in order to catch the lines of moored mines. Soldiers on the rafts would look for mines and then steer their vessels toward them with hopes of catching them. Although the vessels themselves improved, similar in-field searches and grappling hook recoveries were done until World War II. By the 1940s, the development of acoustic and pressure trigger mechanisms outpaced detection technologies and compelled MCM forces to use the "guinea pig" approach of sending in a lead ship to "find" mines (Borden, 2000).

The advancement of sensor technology for mine detection began in the late 1970s and early 1980s, with promising research using helicopter-towed side-scan sonar. Side-scan sonar was first used operationally in 1984 to clear mines in the Red Sea and the Gulf of Suez that had been placed by Libyan dictator Muammar Gaddafi. Rapid developments during the 1980s and 1990s due to various conflicts in the Arabian Gulf lead to the present technologies in use today (Borden, 2000).

b.   *Current Technology*

The stalwart of the USN sonar fleet is the SQQ-32 side-scan sonar which can be mounted on a variety of platforms, including the SLQ-48 submersible. This system is designed to locate moored, tethered or proud bottom mines (PEO LMW, 2009).

For airborne mine detection, the USN operates the MH-53E Sea Dragon helicopter with its suite of aerial MCM tools. The AQS-24 multibeam sonar is the primary mine detection sensor operated by the helicopter. Other devices onboard the helicopter are used to both detect and neutralize simultaneously, including the Mk 105 magnetic sweep, which is towed behind the helicopter and produces a magnetic signature in order to force magnetic influence mines to detonate. The MH-60S helicopter deploys the USN's airborne laser mine detection system (ALMDS), a light detection and ranging

(LiDAR) device with the ability to detect both surface and subsurface mines (PEO LMW, 2009). Since the late 1990s, MCM strategy has included the use of the Coastal Battlefield Reconnaissance and Analysis (COBRA) system, a multispectral video camera operated on an unmanned aerial vehicle (UAV) (Witherspoon, Hollway, Davis, Miller, & Dubey, 1995). BAE Systems and the Naval Surface Warfare Center have recently expanded the spectral toolset of MCM with the development of the Tactical Multispectral Imager (TACMSI) (Louchard, Farm, & Acker, 2008). Both of these multispectral cameras were designed for use at low altitudes over littoral zones (Witherspoon et al., 1995; Louchard et al., 2008).

Navy explosive ordinance disposal divers support MCM detection, using both visual identification and hand held sensors to locate mines. Marine mammal systems, including trained bottle nose dolphins and sea lions successfully detected and neutralized mines during previous Arabian Gulf hostilities (1988, 1991–1992 and 2003) (PEO LMW, 2009).

Other sensors currently being used to detect mines, both academically and operationally, include electromagnetic induction arrays (Barrow & Nelsen, 2001; Malinici, 2004), magnetic gradiometers (Funk, Feldpausch, & Bridge, 2011; Malinici, 2004) and synthetic aperture sonars (Hayes & Gough, 1999).

In recent years the used of unmanned platforms has increased, including remotely operated vehicles (ROV) (both aerial and water-based), automated underwater vehicles (AUV), and UAVs. The USN operates the Remote Multi-Mission Vehicle (RMMV), a semi-autonomous underwater vehicle that uses the AQS-20A side-scan sonar and the AUV Remote Environmental Measuring Unit (REMUS) (von Alt et al., 2001).

While the remote sensing technologies discussed above are reliable and effective techniques for detection of sea mines, they also have important limitations. Each system has a relatively narrow field of view, hindering timely, wide-area searches. Operating a majority of these sensors requires the operator to be placed in harm's way, especially if the targets are within a denied territory. The airborne-based technologies (LiDAR) require low altitudes for the resolution necessary to identify mines and the

water-based technologies (side-scan sonar, multibeam bathymetry) require a vessel to be in the minefield. Systems mounted on AUVs and UAVs may not place soldiers in danger, but have limited operating ranges, further narrowing their search field. Recent developments in high altitude spectral imaging may allow for timely, wide-area surveys to detect mines in denied territories.

B. HYPERSPECTRAL

1. Theory

To understand how hyperspectral imaging (HSI) works, one must first examine the fundamentals of the electromagnetic spectrum. Light is a form of electromagnetic wave and its characteristics are defined by its wavelength. The wavelengths of visible light range from 400 to 700 nanometers (nm), near-infrared wavelengths range from 700 to 1100 nm and short wave infrared wavelengths range from 1400 to about 3500 nm (Jensen, 2008). Figure 1, taken from Shippert (2003) shows the electromagnetic spectrum. Note the called-out section from 400 to 700 nm that denotes the visible spectrum.
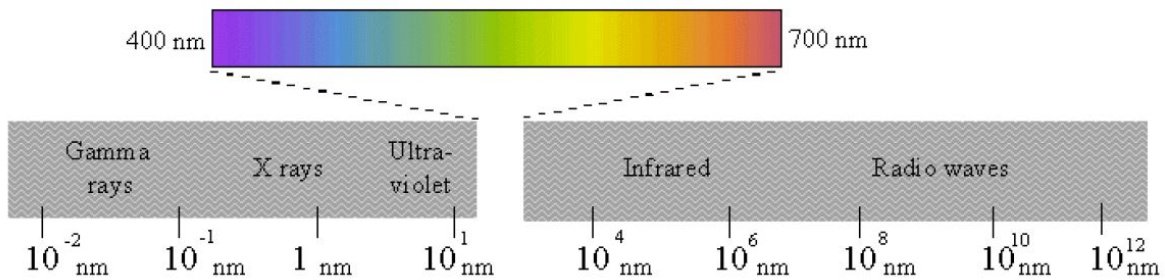
Figure 1.   The electromagnetic spectrum (From Shippert, 2003)

When an electromagnetic wave interacts with a surface it is absorbed by the material, diffusely reflected (scattered) or transmitted through the material (Lillesand & Kiefer, 2000). Imaging spectrometers are passive sensors that measure the intensity of the reflected waves at various wavelengths by using a prism to split the reflected light into individual narrow bands (Jensen, 2008). Hyperspectral spectrometers are imaging spectrometers with the ability to simultaneously record hundreds of individual narrow

(typically 10 nm in width) bands (Goetz, 1996). More specifically, according to Goetz (1992), hyperspectral imaging is defined as the acquisition of images in hundreds of contiguous spectral bands with an ultimate goal to produce a complete reflectance spectrum for each pixel in an image. Taken literally, hyperspectral means "too many bands" and is an oversampling of information in each pixel (Goetz, 1992). This oversampling of information allows for measurement of quantities such as upwelling, radiance, emissivity and reflectance (van der Meer, 2002). Figure 2 shows the concept of imaging spectrometry and the data stack: a two-dimensional representation of a hyperspectral cube, where the 3rd dimension of the cube is the spectral information.
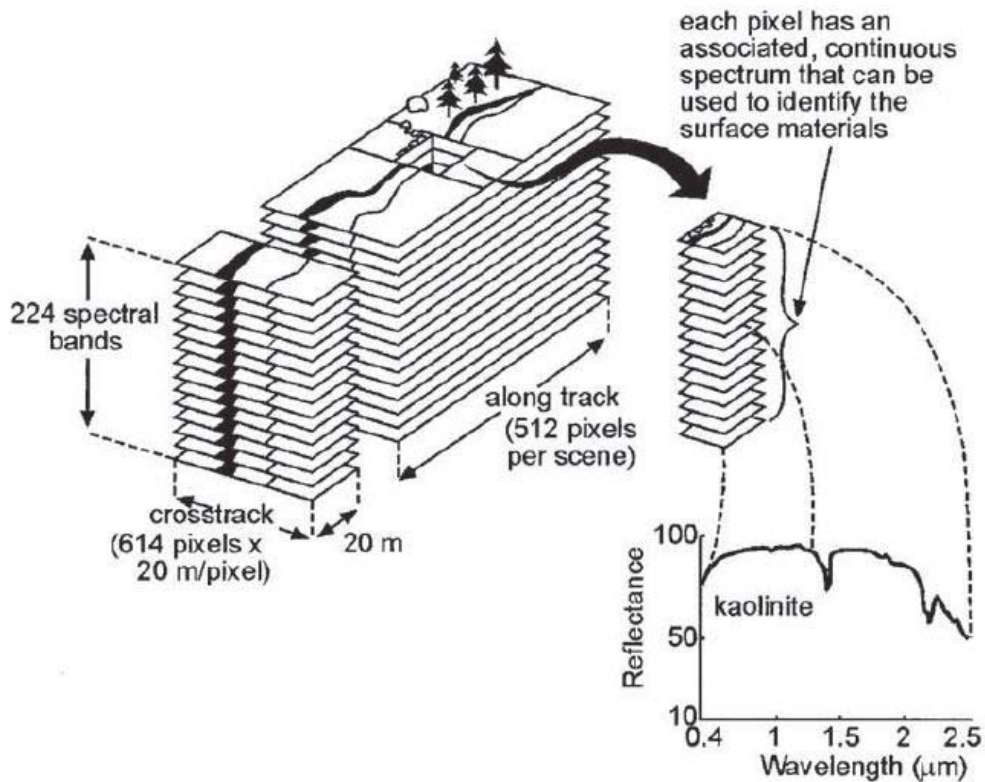
Figure 2.   The basic concept of hyperspectral imaging (From Vane & Goetz, 1988)

a.   *Radiance*

The physical property of a material most precisely measured by a hyperspectral sensor is the material's radiance. Figure 3 shows the concept of radiance,

but to fully understand it a few terms must first be defined. The initial amount of energy incident on a surface per unit area of the surface is the *radiant flux density*. The amount of this energy that is emitted or reflected from this surface, per unit area of the surface is referred to as the *radiant exitance*.   As defined in Equation 1.1, *radiance* is a measurement of the radiant exitance per unit of projected source area in a specific direction and is measured in watts per square meter per steradian:

$$L_\lambda = \frac{\dfrac{\Phi_\lambda}{\Omega}}{A\cos\theta} \quad \text{(W/m}^2\text{/sr)} \qquad\qquad 2.1$$

Radiance (L_λ) and the radiant flux (Φ_λ) are both variable depending on the wavelength. The solid angle, Ω, is a cone-shaped area between the sensor and the surface through which the reflected radiant flux (radiant exitance) has travelled (Jensen, 2008).
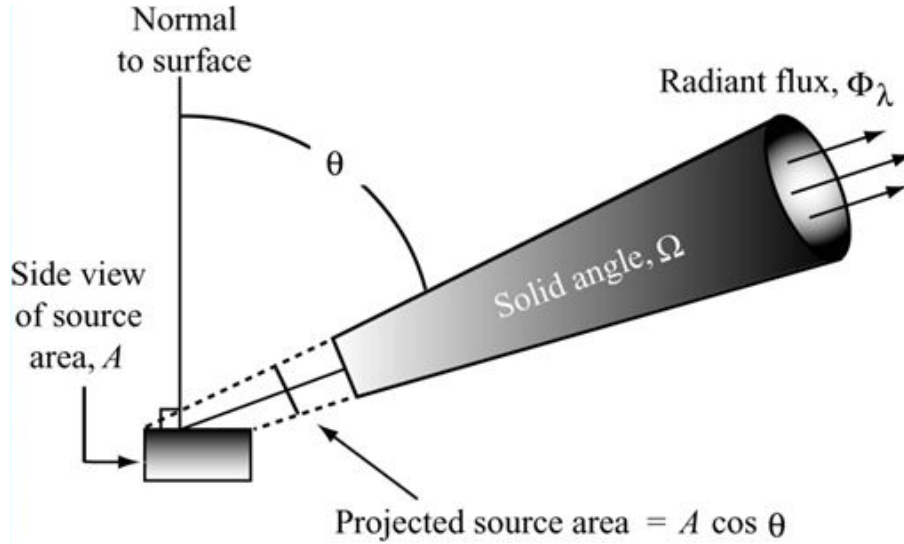
Figure 3.   The concept of radiance and its input variables (From Jensen, 2008)

Unwanted radiometric noise from other sources, including diffuse sky irradiance and radiance from other materials on the ground are introduced into the value recorded by the sensor as the energy travels from the material to the sensor (Jensen, 2008).   Jensen (2008), page 57 gives a detailed description of the variables that factor into the total

11

radiance collected at the sensor. These factors must be accounted for when calculating the true radiance of a material (Jensen, 2008). This radiometric correction process will be discussed in greater detail in Chapter IV.

b. Reflectance

Reflectance is the fundamental physical parameter of a material that hyperspectral imaging attempts to measure for data analysis and interpretation. A hyperspectral image can be converted to reflectance by calculating the ratio of the intensity of the reflected light to the intensity of light that was incident on the surface (van der Meer, 2002; Lillesand & Kiefer, 2000). For a remotely sensed hyperspectral image, the primary factors needed to accurately calculate the reflectance are the variability of illumination factors and the atmospheric effects (Goetz, Boardman, Kindel, & Heidebrecht, 1997).

The amount of energy output by the sun varies with wavelength (Jensen, 2008). Figure 4 shows a typical solar irradiance curve, with the peak in energy occurring in the visible wavelengths. As this curve varies with temperature and time it must be known, calculated or modeled at the time of the image collection (Olsen, 2007).
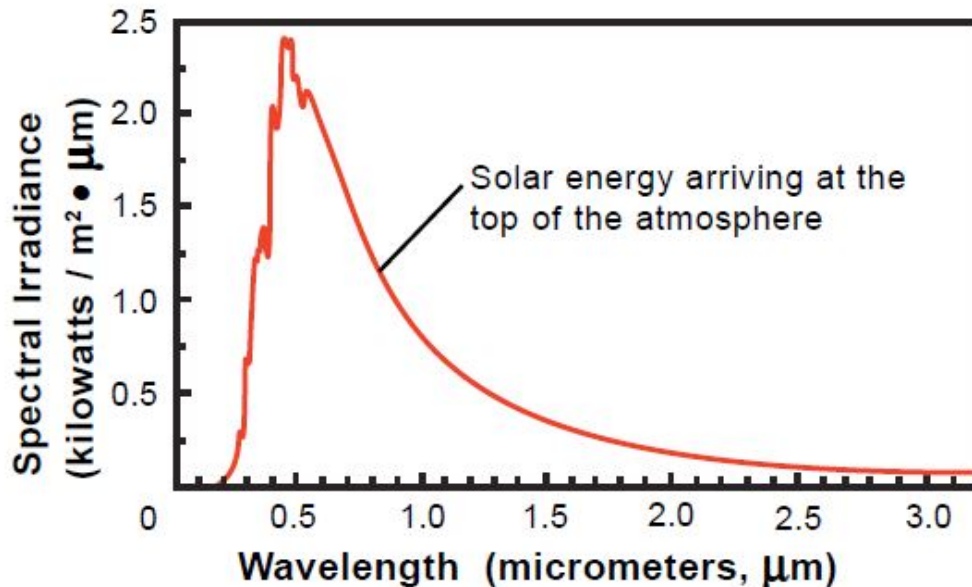
Figure 4.   A typical solar irradiance curve. (From MicroImages, 2001)

One of the key effects the atmosphere has on incoming solar radiation is the absorption of energy at certain wavelengths due to atmospheric gases. This interaction, primarily with carbon dioxide, water vapor and ozone, can reduce the amount of energy that is transmitted or it can absorb it completely (Lillesand & Kiefer, 2000). When certain wavelengths of light interact with aerosols and gas molecules in the atmosphere, the energy is scattered, thus reducing the amount of energy transmitted (Olsen, 2007), A typical atmosphere transmission curve, which has taken into account both scattering and absorption, is show in Figure 5. The absorption bands are the locations where the curve takes a sudden dip downward. Note the complete absorption of energy at 1400 and 1900 nm due to water vapor in the atmosphere. This curve is typically modeled using MODTRAN (Olsen, 2007), but can also be measured using ground-truthed calibration targets (Goetz et al., 1997).
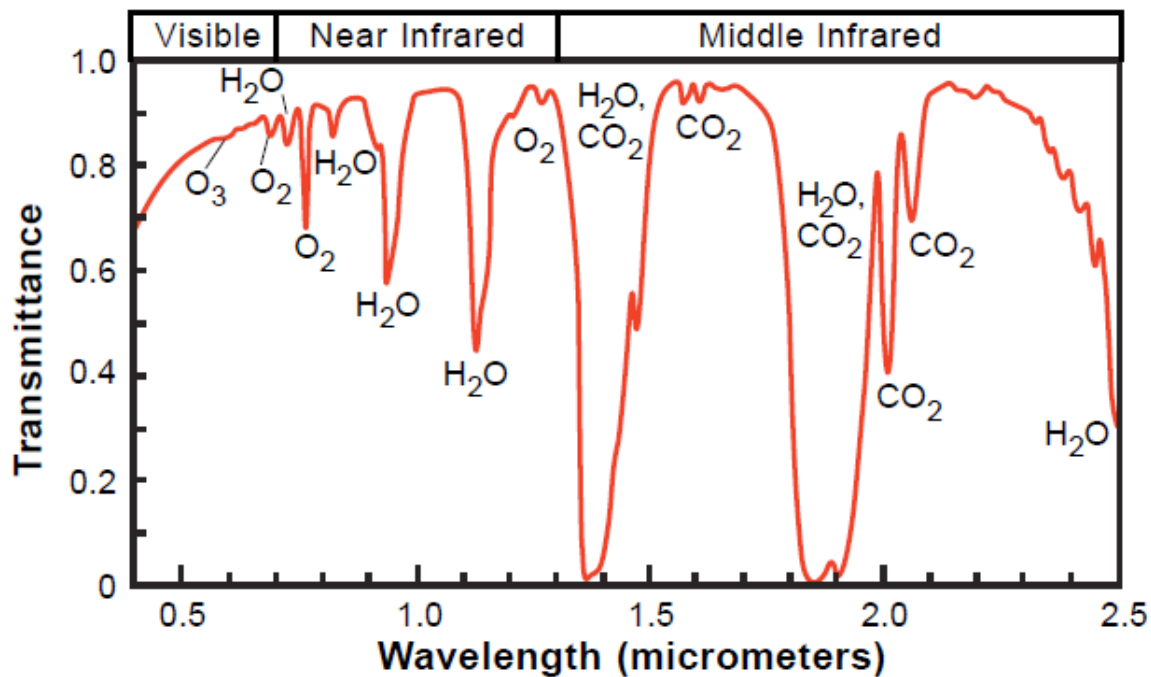
Figure 5. A plot of transmittance versus wavelength for typical atmospheric conditions, showing the atmospheric absorption bands (From Microimages, 2001)

Multiple techniques exist to calibrate a hyperspectral image to derive reflectance, taking into account the variables discussed above. These techniques include empirical methods (Flat Field Conversions, Quick Atmospheric Correction) and modeled

methods (Atmospheric Removal Program) (Goetz et al., 1997). Once a spectrum has been converted to reflectance values, it can be compared to known field or laboratory spectra, making note of the location and shape of the unique absorption characteristics. This can be a difficult process due to inherent spectral variability in all matter. Under precisely the same conditions, identical materials can have slightly different spectra (Lillesand & Kiefer, 2000). Figure 6 shows a typical plot of reflectance spectra created in ENVI, using the United States Geological Survey (USGS) mineral spectral library. The horizontal axis is the wavelength, in microns, while the vertical axis is the calculated reflectance value, which has no units. In this example, the quantitative value of the reflectance has been offset in order to compare the two shown spectra.
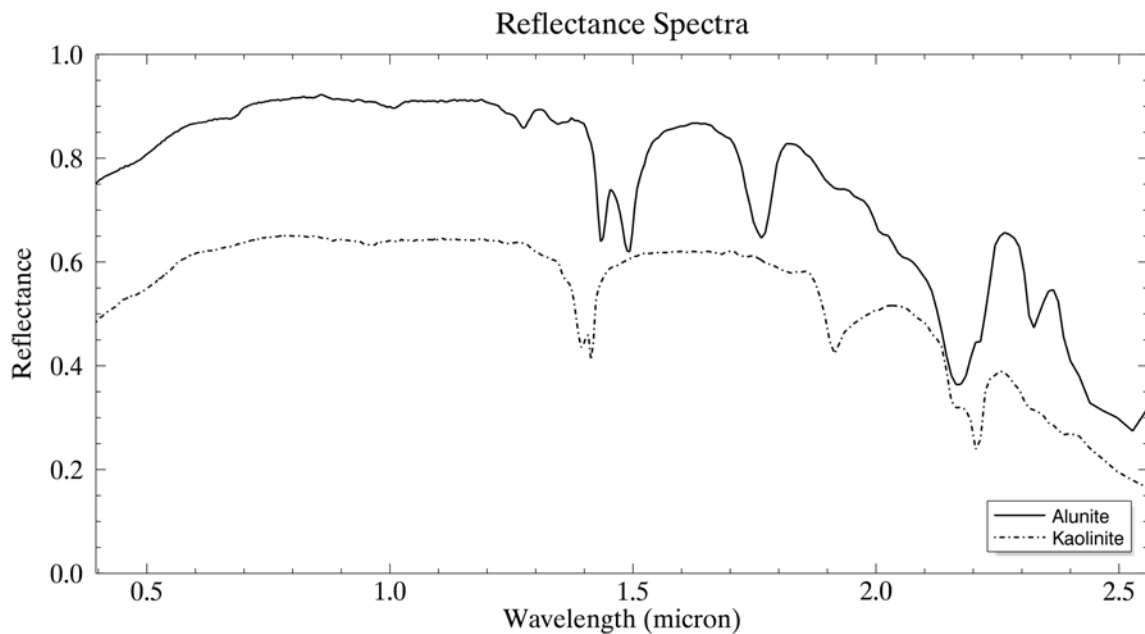
Figure 6.   A typical plot of reflectance spectra (Created in ENVI using a USGS mineral spectral library)

Due to the multitude of information per pixel in a hyperspectral image, a detailed analysis can be done on the data. The narrow, contiguous bands allow for extraction of sub-pixel scale information and the spectral unmixing of a mixed pixel (Boardman, 1993). These concepts will be discussed in detail later in Chapter II.

c.   *Resolution: Spatial vs. Spectral*

To fully understand the capabilities of a hyperspectral sensor, one must first understand the difference between spatial and spectral resolution. Spatial resolution is the smallest distance between two ground points such that both points can be resolved by the sensor (Jensen, 2005). For example, a 1 meter resolution imaging system would be able to image a 1x1 meter target on 1 pixel. Ground sample distance (GSD) and spatial resolution are often used interchangeably, although a truer definition of GSD is a measurement of the ground distance between the points imaged on the center of adjacent pixels (Olsen, 2007).

Spectral resolution, as described by Jensen (2005), "is the number and dimension (size) of specific wavelength intervals . . . in the electromagnetic spectrum to which a remote sensing instrument is sensitive" (p. 14). The spectral resolution of a sensor is often defined by the full-width at half maximum (FWHM) of the gaussian curve representing the detector sensitivity (Clark, 1999). As an example, the high spectral resolution hyperspectral instrument Airborne Visible / Infrared Imaging Spectrometer (AVIRIS) has a spectral resolution of 10 nm (Green et al., 1998). Figure 7 illustrates the FWHM concept and the gaussian curve that represents a detector's spectral sensitivity.
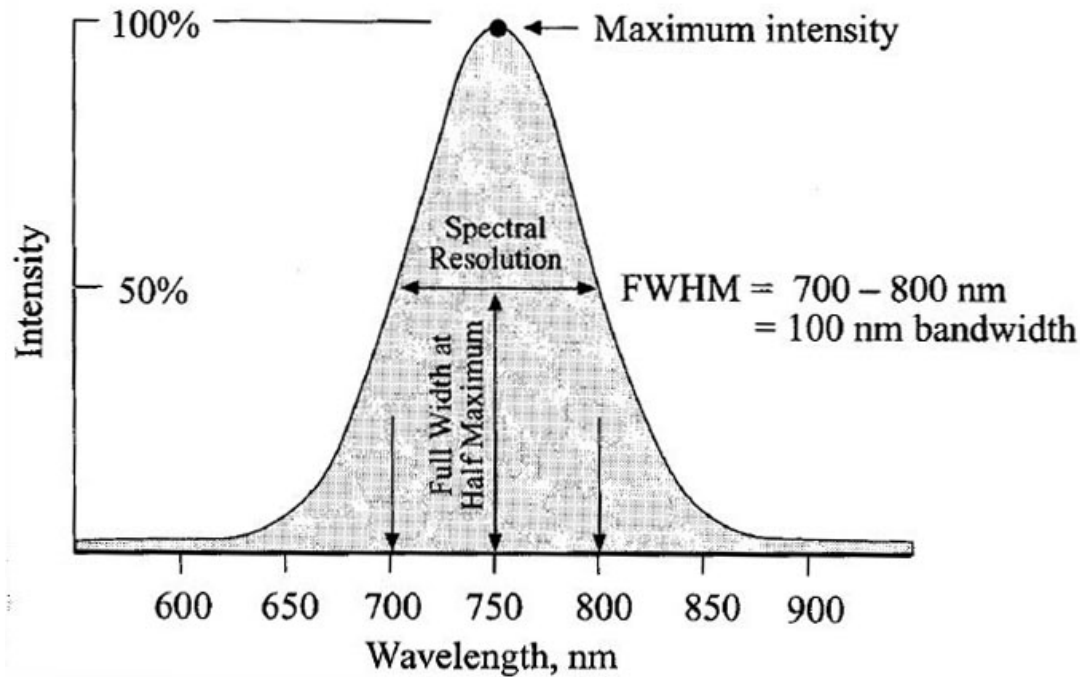
Figure 7.   A measure of spectral resolution using the FWHM of a detector's gaussian
sensitivity curve (From Jensen, 2005)

2.   History of Hyperspectral Remote Sensing

The origins of remotely sensed imaging spectroscopy can be found in the mineral industry, using the technology as a tool to create geologic maps (Goetz, Vane, Solomon & Rock, 1985). By the late 1980s, airborne hyperspectral instruments became a reliable tool, with the development of the Jet Propulsion Laboratory's (JPL) AVIRIS and ITRES Research Ltd.'s Compact Airborne Spectrographic Imager (CASI) (Kruse, 1999). In recent years, commercial developments have seen hyperspectral imaging applied to forestry, resource management, geology, physics and agriculture (van der Meer & De Jong, 2002). Militaries have begun to use this technology in support of intelligence, surveillance and reconnaissance (ISR) applications, including target detection and material identification. Currently, the U.S. Air Force (USAF) has committed funds to

16

Raytheon's Airborne Cueing and Exploitation System, Hyperspectral (ACES-HY) and Goodrich's Spectral Infrared Imaging Technology Testbed (SPIRITT), among others (Butler, 2011).

3.   Physics of Hyperspectral Imaging and Water

High resolution imaging over water can be difficult due to the unique variables marine environments introduce into hyperspectral measurements. Trying to look below the surface at objects submerged in the water can be even more complicated (Hedley, Harborne, & Mumby, 2005).

a.   Water and Radiance

As discussed earlier, the total radiance recorded at a sensor includes unwanted radiometric noise from additional sources. These sources include reflected radiance from other ground sources and downwelling irradiance from both the sun and the sky.   A simplified radiance model is shown in Figure 8 illustrating the additional factors that must be taken into account when looking into the water column. These new factors are the initial reflection off of the surface of the water (L_s), the reflection off of the particles or objects in the water column (subsurface volumetric radiance) (L_v) and, if shallow enough, the reflection off of the underlying substrate (L_b) (Bukata, 1995). When trying to spectrally analyze objects in the water column, the subsurface volumetric radiance has to be extracted from the total radiance (Doxaran, Froidefond, Lavender, & Castaing, 2002).
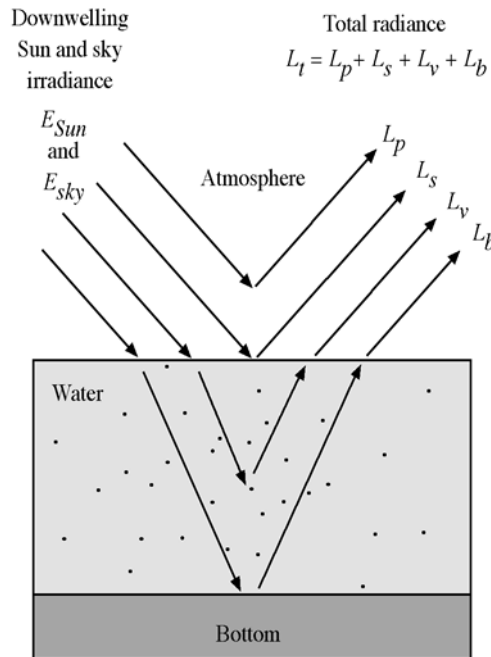
Figure 8.   A diagram showing the additional radiance factors added to the total radiance when looking into water (From Jensen, 2008; modified from Bukata, 1995) L_t is the total radiance and L_p is the downwelling irradiance from the sun and sky

b.   *Absorption and Scattering*

As light travels through water it is scattered and absorbed by the water molecules. Figure 9 illustrates the absorption and scattering coefficients of pure water as a function of wavelength. This image is an inverse of the transmission curve shown earlier, with a lower value representing a higher amount of transmission. Wavelengths greater than 520 nm are heavily absorbed by water, with the near-infrared wavelengths (greater than 750 nm) almost completely absorbed. Wavelengths less than 400 nm are both absorbed and scattered. The least amount of scattering and absorption occurs in the 400–500 nm range, with the minimum at about 460 nm. These blue / blue-green wavelengths are transmitted efficiently in pure water and thus penetrate further into the water column than other bands (Lillesand & Kiefer, 2000). This makes them ideal wavelengths to look into *pure* water (Jensen, 2008).

Absorption and Scattering Attenuation in Pure Water
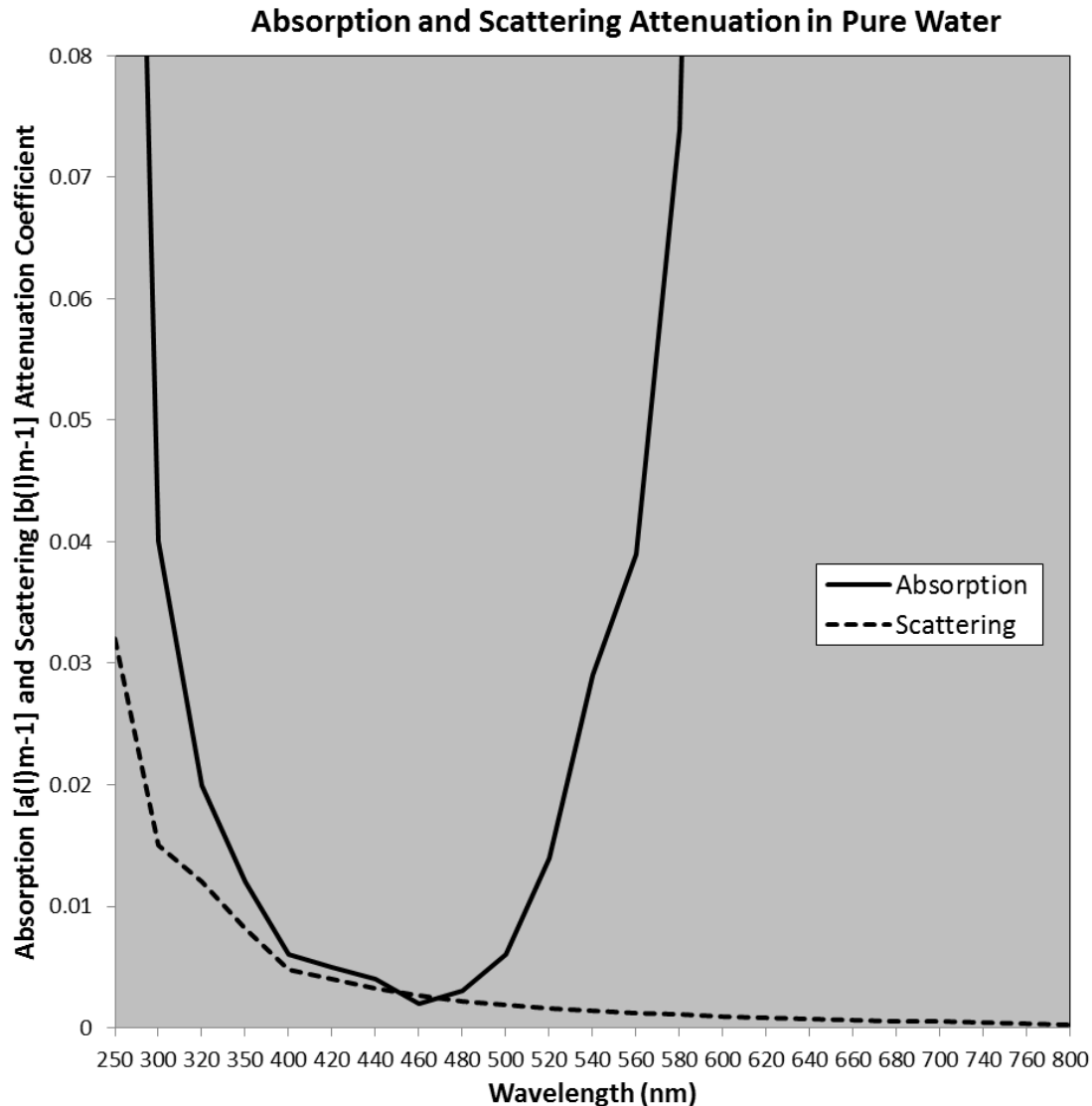
Figure 9.   The absorption and scattering of light as a function of wavelength. Note the minimum at 460 nm (Modified from Jensen, 2008, original data derived from various sources by Bukata, 1995)

Pure water, containing only water molecules, does not exist in nature. Real water contains a variety of dissolved and particulate biological and inorganic matter. These impurities will alter the reflected spectrum, as well as the absorption and scattering coefficients shown in Figure 9. Some of the impurities have a negligible effect, while others have a much larger effect. Dissolved salt for instance, can increase scattering by 30% as compared to pure water (Mobley, 1994).   Table 1 defines some common

constituents in water and the effect they have on light propagation in water. "Variant upon concentration levels of dissolved substances . . . the total spectral absorption [and scattering] coefficient for any water sample will range from that of pure water to ones that show orders of magnitude greater than pure water" (Blankenship, 2006, p. 28). Much like the atmospheric effects discussed earlier, water column effects must be modeled or measured (using systems such as the portable profiling oceanographic instrument system) to truly understand the spectral response of objects in the water column (Mobley, 1994; Stein, Schoonmaker, & Coolbaugh, 2001).

Table 1.   Common constituents in water (From Blankenship, 2006, modified from Mobley, 1994)

Type of Particle	Size of Particle	Contribution to Light Propagation in Water
Organic Particles		
Viruses	20-250 nm	Due to their size, viruses tend to be inefficient absorbers and scatters. However, there is the possibility of a significant contribution to the backscatter coefficient b_b in the blue wavelengths.
Colloids	0.4-1.0 μm	Significantly contribute to backscattering
Bacteria	0.2-1.0 μm	Significant scatters and absorbers especially at blue wavelengths and in clear oceanic waters.
Phytoplankton	<1 - >200 μm	Primarily responsible for determining the optical properties of most oceanic waters and contribute very little to backscatter.
Detritus	<1 - >20 μm	Residues of decomposed cells of phytoplankton and are major backscatters in the ocean.
Inorganic Particles		
Quartz Sand	0.1 - >100 μm	Very finely ground sand that results from erosion.
Clay Minerals	0.1 - >100 μm	Wind blown dust usually from coastal waters.

c.   *Transmission and Refraction*

Transmission occurs when electromagnetic waves pass through a medium. When the waves are transmitted from a medium of one density to another medium (e.g.

air to water), refraction occurs. This deflection of light alters the velocity and wavelength of the wave and creates a "blurring effect." The magnitude of this change is defined by Snell's Law:

$$n_1 \sin \theta_1 = n_2 \sin \theta_2 \qquad\qquad 2.2$$

where *n* represents the index of refraction for the two media and θ is the angle of transmittance (Olsen, 2007).

d.   *Glint*

The main complication of imaging over water is the presence of sun glint in an image. Glint, sometimes referred to as clutter, is a result of specular reflection of direct solar radiance off of wave crests (Hochberg, Andrefouet, & Tyler, 2003). As seen in Figure 10, this phenomenon appears as extremely bright pixels and obscures all spectral information about the reflecting surface (Kutser, Vahtmae, & Praks, 2009). As such, glint mitigation is essential for spectral studies in marine environments.

The most effective form of mitigating glint is to avoid it by planning data collections such that the position and angle of the sensor with regards to the sun angle minimizes the glint (Hochberg et al., 2011). According to Mustard, Staid and Fripp (2001) this can be achieved with an aerial collection by flying towards or away from the sun, with solar elevation angles between 30° and 60°. Figure 10 is an example of the difference solar elevation angle can make with regards to glint in a hyperspectral image. The two images are of the same geographic location and were collected by the same sensor. The left image was collected early in the morning, with a solar elevation angle of approximately 43° and the right image was collected mid-day, with a solar elevation angle of greater than 60°. As expected, the right image is heavily saturated with glint and the left image is not. Collecting data when the sea state is calm will also reduce the amount of glint by reducing the number of surfaces for specular reflection (Hochberg et al., 2011).
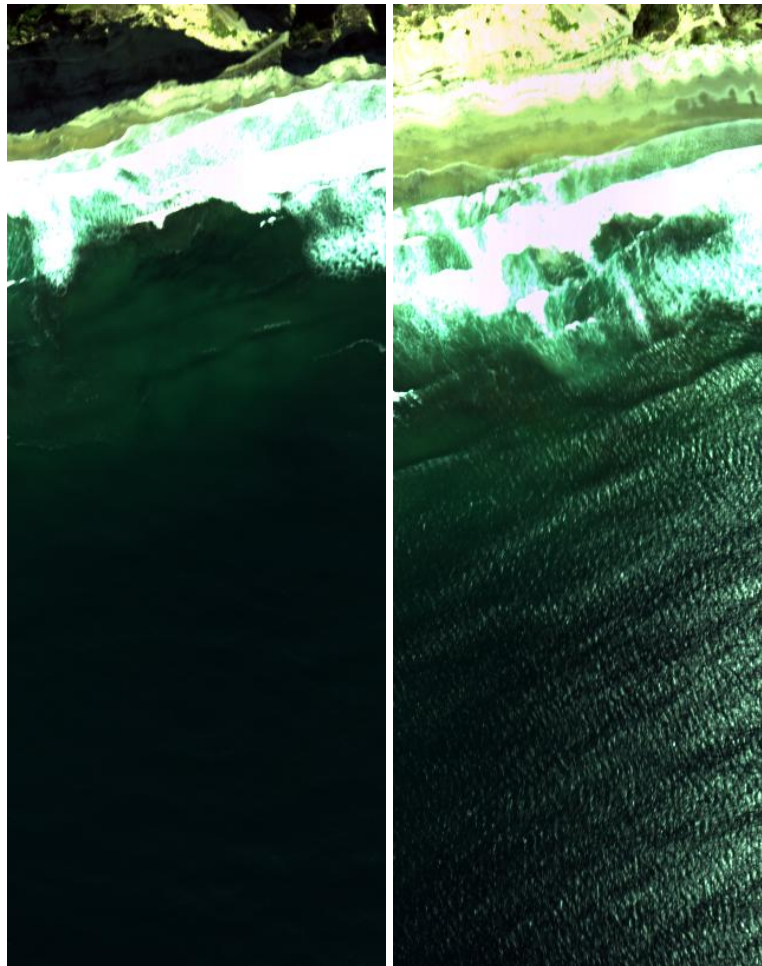
Figure 10.	True color composite images (R: 641 nm, G: 551 nm, B: 460 nm) from ProSpecTIR-VS3 illustrating the effect solar elevation angle has on glint. Both images were recorded by the same sensor, with the left image being recorded early in the morning and the right image recorded mid-day

Although glint can obscure the spectral signal it is possible to recover the component resulting from the reflecting surface (Hedley et al., 2005). Much research has gone into the development of algorithms for removing glint from images, starting with Cox and Munk (1954). They analyzed aerial photographs in order to make quantitative measurements of sea surface roughness and the slope of waves at various wind speeds. This statistical model-based approach allows for glint correction over large areas, using low resolution sensors (on the order of 100s to 1,000s of meters). As this technique uses

a very basic model, it does not translate well to marine environments with large variability in sea surface (i.e. littoral zones) nor does it accurately correct for high resolution images (Vahtmae & Kutser, 2008).

Barnes, Gilbert, Schoonmaker and Rohr (1999) successfully used a processing technique to look at *large* objects in the water column. Due to the absorption and reflection characteristics of surface phytoplankton, the covariance between a green and blue band was defined as the sea surface. The variance of a green band was then divided by the covariance of the two bands. This green band weighted average was then subtracted from the blue band, removing the water surface and allowing one to "see" humpback whales in the water column (Barnes, Gilbert, Schoonmaker, & Rohr, 1999). Figure 11, although low resolution, shows the ability of spectral processing techniques to greatly enhance the imaging ability of submerged objects. Although successful in this example, this technique required the whales to be relatively shallow and at a precise angle to the sun, due to their highly reflective grey and white bodies. Additionally, this process is highly susceptible to surface clutter, including wave crests (Barnes et al., 1999).
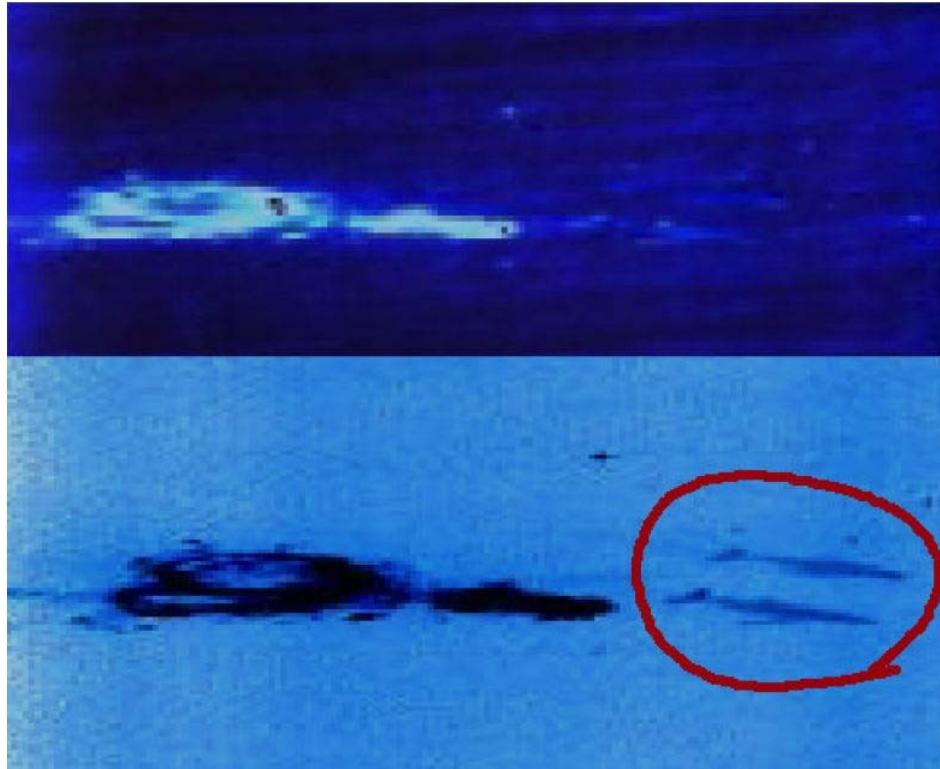
Figure 11.   Images demonstrating spectral processing's ability to look into the water column. The top image is an unprocessed true color image, showing the ocean surface with the white cap of a breaking wave. The bottom image has been processed using the technique described in the text above. Note the obvious humpback whales to the right (Originally from Barnes et al., 1999, modified by Potter, 1999)

Recently developed methods to remove glint involve a direct estimation of the amount of glint in each image, allowing for correction of higher resolution images, with more spatial variability in the sea surface state (Hochberg et al., 2011). Hochberg, Andrefouet, and Tyler (2003) took advantage of the fact that infrared (IR) light is strongly absorbed by water and thus any IR radiance recorded after atmospheric corrections would come solely from the surface of the water. The amount of glint in the IR bands is then assumed to be linearly related to the amount of glint in visible bands. A glint value is then estimated by subtracting the darkest pixel in an image from the brightest. This value is then subtracted from each pixel (Kay, Hedley, & Lavender, 2009). Others, including Silva and Abileah (1998) and Hedley, Harborne, and Mumby. (2005) continued to refine this approach. Kutser, Vahtmae, and Praks. (2009) suggested

24

a slight variant of the method by using the depth of the oxygen absorption band at 760 nm to define the amount of glint.

C.   SPECTRAL ANOMALY DETECTION

As the altitude of collection increases, pixel size relative to the target decreases. Due to the relative small size of naval mines, using an airborne hyperspectral sensor to detect them can be difficult. Whereas larger targets tend to encompass multiple pixels even when imaged from high altitude, mines tend to be sub-pixel in size and thus their observed spectrum is a mixture of both background and target spectra. In order to detect sub-pixel mines, spectral mixing models must be defined and spectral anomaly detectors must be used (Winter, 2008). This has been a widely researched topic, with Singer and McCord (1979) determining that macroscopic scale mixing is linear and Nash and Conel (1974) finding that microscopic scale mixing occurs nonlinearly. Although a simplification of the complicated contributors to a *pixel* spectrum, a common technique is to assume the mixing occurs linearly (Boardman & Kruse, 2011).

1.   Mixture Tuned Matched Filtering

Mixture Tuned Matched Filtering (MTMF) is a popular dual-threshold detector that is readily found in ENVI (Boardman, 1998). MTMF combines the linear spectral mixing model and statistical matched filtering (MF), a technique commonly used in signal analysis to extract known signals from a mixed background (Boardman, 1998; Boardman & Kruse, 2011). According to Boardman (1998), "[t]he MTMF method leverages the high dimensionality of [hyperspectral] data, using the high dimensional space to its advantage, to greatly increase detectability and selectivity" (p. 55), as well as decrease false-positive rates. The advantage of MTMF as compared to other spectral mixture models is MTMF's ability to un-mix a pixel with a priori knowledge of just one endmember spectrum (the target of interest), whereas other models require all of the endmembers to be known (Boardman, 1998; Boardman & Kruse, 2011). Although a strength compared to other spectral mixing models, this required a priori knowledge could hinder MTMF's robustness, due to potential target spectral variability (Stein et al,

2002). A detailed analysis of the theory and algorithms of MTMF can be found in Boardman and Kruse (2011). Figure 12 displays a list of the MTMF processing steps, modified from Boardman and Kruse (2011). In the following text a few of the major steps are discussed in greater detail, as well as some of the previous studies that have used the MTMF method.

```
┌────────────────────────────────────────────────────────────────┐
│                      MTMF PROCESSING STEPS                      │
│ 1. Preprocessing and Data Conditioning (Minimum Noise Fraction  │
│    [MNF])                                                       │
│         a. Estimation of noise covariance matrix               │
│         b. Data subjected to noise whitening transform         │
│         c. Mean subtracted from noise-whitened data            │
│         d. Noise-whitened data projected onto its eigenvector, │
│            decorrelating it                                     │
│ 2. Matched Filtering for Abundance Estimation (MF Projection)  │
│         a. Target spectrum transformed to MNF space            │
│         b. Background covariance matrix estimated and inverted │
│         c. Normalized matched filter projection vector         │
│            calculated                                          │
│         d. MNF data projected onto MF vector to estimate       │
│            target abundance                                    │
│ 3. Mixture Tuning to Measure Feasibility (MT Modeling)         │
│         a. Continuum of mixture distributions interpolated     │
│         b. Mixture infeasibilities calculated for each pixel   │
│         c. Valid detections separated from false positives     │
└────────────────────────────────────────────────────────────────┘
```

Figure 12.   The processing steps of the Mixture Tuned Matched Filter (Modified from Boardman & Kruse, 2011)

a.   Data Reduction

(1) Minimum Noise Fraction. In order to isolate noise in highly dimensional data from the background and target spectral signatures, a minimum noise fraction (MNF) transform is run prior to MTMF. MNF was initially developed by Green, Berman, Switzer and Craig (1988) to determine the "inherent dimensionality of the data . . . using a special orthogonalization procedure related to principal components" (Boardman & Kruse, 2011, p. 4140). This transformation isolates the large eigenvalues (the data) from the small ones (the noise) (Green, Berman, Switzer, & Craig., 1988).

(2) Pixel Purity Index. After a MNF transform is run, the data are further reduced by processing the most significant MNF bands using a pixel purity index (PPI). The data are projected into *n*-dimensional scatter plots to identify the purest spectral endmembers (Boardman & Kruse, 2011).

b.   *Output*

The MTMF method outputs a matched filter (MF) score image and an infeasibility image. The MF score image is a per pixel abundance estimation of the target spectrum, giving pixels dominated by the background spectra a score of 0 and pure target pixels a score of 1. The infeasibility image is a per pixel score of the likeliness of the pixel spectrum to be a mixture of the background spectrum and the target spectrum. This value is calculated by the MT part of MTMF, measuring the vector distance of the pixel from the line segment connecting the target spectrum and the background mean (Boardman & Kruse, 2011).

c.   *History of Use*

This heavily tested technique has been used successfully in Kruse (2003, February), Kruse, Boardman and Huntington (2003), Mars and Crowley (2003), Winter (2008), DiPietro (2010), DiPietro et al. (2010), and Boardman and Kruse (2011), among others.

2.   Reed-Xiaoli Anomaly Detector

Due to the variability of potential target spectra, an anomaly detector that simply distinguishes unusual materials from a background material, without a priori knowledge of the target spectrum is advantageous (Stein et al., 2002). These targets are then defined in reference to the overall background characteristics.

Reed and Yu (1990) developed the Reed-Xiaoli (RX) anomaly detector (Yu, Reed, & Stocker, 1993; Yu, Hoff, Reed, Chen, & Stotts, 1997). This widely used, local spectral anomaly detection algorithm was originally designed for multispectral data, but has since shown its applicability to hyperspectral data as well (Stein et al., 2002; Chang & Chiang, 2002; Kwon & Nasrabadi, 2005). RX detection algorithms are optimal for locating targets in water due to the relatively homogenous Gaussian background of the ocean surface (Winter, 2008). RX detectors (RXD) exploit the spectral difference between a specific pixel and the surrounding background pixels (Kwon & Nasrabadi,

2005), calculating the Mahalanobis distance. This is done by using the local clutter mean and covariance of the surrounding pixels (Winter, 2008).

A version of the RXD used in ENVI implements a background subtraction algorithm known as the Uniform Target Detector (UTD) to improve the performance of the RXD (Chang & Chiang, 2002). This RXD-UTD method was shown to be effective by Ashton and Schaum (1998) and applies the following formula to each pixel:

$$\delta_{RXD-UTD}(r) = (r-1)^T K_{LxL}^{-1} (r-\mu) \qquad\qquad 2.3$$

where $\delta_{RXD-UTD}(r)$ is the RXD-UTD target score, K_{LxL}^{-1} is the sample covariance matrix of L by L dimensions, r is the pixel spectral vector and μ is the mean spectral vector of the area of interest. The output of running this detector is a matrix of confidences for each pixel (Chang & Chiang, 2002).

The limitation of RX anomaly detectors is their susceptibility to high false alarm rates due to isolated spectral anomalies (Winter, 2008) and the assumption that the background is homogenously gaussian (Stein et al., 2002). Additionally, due to the high dimensionality of hyperspectral data, running RX detector algorithms on HSI images can be computationally intensive. This is owed to the need to calculate the inverse of large covariance matrices (Banerjee, Burlina, & Diehl, 2006).

a.   *History of Use and RX variants*

Muise (1996) used the COBRA multispectral sensor to detect individual mines with an algorithm based on the RX anomaly detector. Very similar work was done by Louchard et al. (2008) with TACMSI, but with the added ability to multi-look, mitigating transient (generally glint-caused) false alarms.

3.   **Various Other Anomaly Detectors**

Automated sub-pixel target detection research has been done previously by Acker, Pfeiffer, and Farm (2003) using the Littoral Airborne Sensor, Hyperspectral (LASH). Acker et al. (2003) used the LASH Stochastic Mixing Model algorithm, a

modified version of the Finite Target Matched Filter model designed by Stocker and Schaum (1997).   This real-time automated detection algorithm determines pixel constituents with statistical probability curves and requires an input target spectrum. Acker et al. (2003) had positive results compared to traditional methods, with high target detection rates and low false positive rates (<1 per hour).

Other anomaly detection algorithms include the Gauss-Markov Random Field (GMRF) algorithm developed by Schweizer and Moura (2000) and the Support Vector Data Description (SVDD) from Banerjee, Burlina and Diehl (2006).   These algorithms are extremely similar to the techniques previously described, albeit altered to address errors caused by assuming a gaussian and homogenous background.   GMRF and SVDD assume the background clutter to be spatially and spectrally random (Schweizer & Moura, 2000; Banerjee et al., 2006).   Still others have found success with techniques including principle component transformations (Miao et al., 1998) and the low probability detector (LPD) (Harsanyi, Farrand, & Chang, 1994), similar to the UTD (Chang & Chiang, 2002).

THIS PAGE INTENTIONALLY LEFT BLANK

III.   DATA COLLECTION AND GROUND TRUTH FIELD WORK

A.   COLLECTION

The data for this project were collected on March 20th and 21st, 2012, over a United States Navy barnacle study test range offshore La Jolla, California. With the unavailability of the SPIRITT hyperspectral sensor, SpecTIR, LLC, a privately owned remote sensing firm out of Reno, Nevada was contracted to collect hyperspectral images of the test range. Their ProSpecTIR-VS3 instrument was used as a proxy for the SPIRITT sensor and was flown on a low altitude Cessna 206 single engine aircraft.

1.   Targets

Six 0.8 meter diameter targets were deployed by Scripps Institution of Oceanography into the Navy test range. Water depths in the range varied from 34 to 48 meters. Three of the targets were painted green and submerged to 3 meters, 2 meters and 1 meter below the surface, respectively. The other three targets were left on the surface and painted white, green or black. Additionally, as shown in Figure 13, the test range boundaries were marked by a variety of surface buoys with sub-meter diameters. The northwest and southwest buoys were connected to 3 additional buoys, half meter in size and painted black, blue and green. Additional descriptions of the targets are available in the classified addendum to this report.

Figure 13.   Target locations overlaid on a true-color WorldView-2 Image.

a.   *Additional Targets*

During data collection, the author and scientists from Rochester Institute of Technology and Goodrich ISR ran hyperspectral calibration experiments near the test site. These experiments included the use of four 2 x 2 meter black and grey calibration panels, a 5.5 meter Zodiac and the 33.5 meter M/V Merlin. These elements are present in the images.

2.   Airborne Sensor Description

The pushbroom-imaging ProSpecTIR-VS3 is a dual sensor instrument that contains a visible and near-infrared (VNIR) sensor and a short-wave infrared sensor (SWIR). The VNIR sensor can record 244 unique spectral bands covering the spectral

range of 400 to 1000 nm and the SWIR sensor can record 254 bands over the spectral range of 970 to 2500 nm. The VNIR and SWIR sensors have spectral resolutions of 2.9 and 8.5 nm, respectively. The VNIR sensor uses a silicon charge-coupled device (CCD) focal plane, while the SWIR sensor has a mercury cadmium telluride CCD (SpecTIR, LLC, 2011).

ProSpecTIR-VS3 is operated on a Cessna 206 aircraft and is pointed to nadir with a 24° field of view (FOV). The instrument is integrated with flight operations by an internal global positioning system (GPS) receiver with inertial navigation system (INS) and inertial measurement unit (IMU) sensors (SpecTIR, LLC, 2011). Figure 14 shows the ProSpecTIR-VS3 instrument and Figure 15 shows its typical specifications.

Figure 14.   The ProSpecTIR-VS3 hyperspectral sensor (From SpecTIR, LLC, 2011)

PROSPECTIR –VS TYPICAL SPECIFICATIONS								
SPECTRAL RANGE	VNIR 400-970 nm				SWIR 970-2450 nm			
	Total 400-2450 nm							
SPECTRAL RESOLUTION (OPTICAL)	VNIR 2.9 nm				SWIR 8.5 nm			
SPECTRAL CHANNELS	~360 typical operation, 500 at highest resolution							
SPECTRAL BINNING CONFIGURATION	VNIR	1x	2x	4x	SWIR	1x	2x	4x
SPECTRAL CHANNELS		244	122	60		254	127	63
SPECTRAL SAMPLING (nm)		2.3	4.6	9.2		5.8	11.6	23.2
TERRAIN COVERAGE & FIELDS OF VIEW								
SPATIAL PIXELS	320							
FOV	24 degrees							
IFOV	0.075 degrees (1.3mrad)							
OPERATIONAL CHARACTERISTICS								
CAMERA A/D	VNIR	Si CCD 12 bits			SWIR	MCT 14 bits		
SNR	500:1 typical, 750:1 peak				650:1 typical, 1100:1 peak			
INTEGRATION PERIODS	adjustable at each sensor for optimum exposure levels							
IMAGE RATE	Up to 100 images/s							
MECHANICAL								
DIMENSIONS	25 x 19 x 16 inches (HWD)							
WEIGHT	50kg sensor							
ENVIRONMENTAL								
TEMPERATURE	+5°C to + 35° C Operational | +5°C to + 45° C Storage							
HUMIDITY	5 – 95% Operational | 5-95% Storage							
VIBRATION	15-2000 Hz, 10 min (transportation) 10 – 2000 Hz, 0.5g, 2 Oct/min (resonance) [MIL-STD-810G Method 514.6. Procedure 1]							
SHOCK	20g, 11ms, sawtooth pulse [MIL-STD-810G Method 516.6 Procedure 1]							

Figure 15.   Typical specifications of the ProSpecTIR-VS3 hyperspectral sensor (From SpecTIR, LLC, 2011)

3.   Collection

a.   *Flight Line Plan*

As discussed previously, the spatial resolution of the images is dependent on the altitude of the sensor. In an effort to collect both a high spatial resolution and a low spatial resolution data set, two flight altitudes were planned. The high spatial resolution collection altitude was approximately 410 meters and the low spatial resolution altitude was approximately 800 meters. The spatial resolutions of the collections were 0.5 and 1.0 meters, respectively. The flight line spacing was planned such that each

image provided 35% overlap with adjacent images. This resulted in a plan of 17 collection lines for the high spatial resolution images and 7 collection lines for the low spatial resolution images. Figures 16 and 17 show the planned flight lines for the high and low spatial resolution collections, respectively. Appendix A shows the detailed flight plan spreadsheets for each of the collections.

Figure 16.   Planned flight lines for the high spatial resolution collection (From Goodrich ISR Systems, 2012)

Figure 17.   Planned flight lines for the low spatial resolution collection (From Goodrich
ISR Systems, 2012)

b.   Collection Process

The low spatial resolution flight lines were flown on March 20th, 2012
from 09:28 to 10:42 local time (PDT) at a rate of 100 knots. The high spatial resolution
lines were collected on March 21st, 2012 from 09:12 to 10:06 PDT at a rate of 80 knots.
In an attempt to mitigate solar glint off the water, lines were flown in the morning with a
low solar elevation angle of approximately 43 degrees. Data were collected during the
afternoons of March 20th and 21st as well, but the sensor was over-saturated with glint,
rendering the data unusable.

For each resolution, lines were collected while heading the same direction
in order to prevent bidirectional reflectance distribution function (BRDF) artifacts. For
the low spatial resolution collections, the lines were flown west to east and for the high
spatial resolution collections, the lines were flown east to west. All data were collected

during optimal weather conditions—sunny and clear. Each high spatial resolution image is approximately 3,400 meters long by 160 meters wide and each low resolution image is 3,400 meters by 330 meters. All collected data contain 360 spectral bands ranging from 390 to 2465 nm. The wavelength of each band is listed in Appendix B.

In order to save time only lines 5 through 13 were flown while collecting the high resolution images. Lines 1 through 4 and 14 through 17 were deemed unnecessary as they were outside the target area. All 7 planned low resolution lines were flown.

THIS PAGE INTENTIONALLY LEFT BLANK

IV. PROCEDURES

A. SPECTIR, LCC PRE-DELIVERY DATA PROCESSING

1. Radiance Calibration and Conversion

Prior to delivery to the Naval Postgraduate School, the data were radiometrically calibrated using a Labsphere USS-2000-V uniform source, allowing for the data to be accurate within 5% of absolute radiance. The wavelength measurements were calibrated with an Oriel Cornerstone 130 1/8m monochromator and are accurate to within 0.5 nm (SpecTIR, LLC., 2012).

Using dark measurements recorded at the end of each flight line and a SpecTIR proprietary compensation algorithm, dark current signals (sensor noise) were removed from the data. The previously created calibration gain file was then used to convert the raw data to radiance units (SpecTIR, LLC., 2012). These radiance files were then delivered to the Naval Postgraduate School in .dat ENVI file format, along with the associated header files.

2. GLT Creation

SpecTIR's flight package included a fully integrated INS and IMU. To allow for accurate georeferencing of the data, the IMU provided real-time differential corrections to the INS. Prior to flight, a boresight calibration test was completed, ensuring "optimal translation of the INS positional data to the image" (SpecTIR, LLC., 2012, p. 8).

For each collected flight line, this geo-location information was encoded into both an internal geometry map file (IGM) and a geographic lookup table (GLT). The IGM is a pixel identification file consisting of easting and northing values in separate bands. The GLT contains 2 bands which point the non-geometrically corrected data into map space, with a UTM Zone 11 projection and a WGS-84 datum. Both of these file types were delivered with their respective data files to the Naval Postgraduate School.

B.   VISUAL INSPECTION OF THE DATA

1.   Flight Line Selection

Using ArcGIS, the known locations of the targets were plotted into a point shape file. Geocorrected tiff images of the high and low resolution flight lines were created and brought into ArcMap, along with the target locations. The high spatial resolution (0.5 meter) flight lines were used for target location verification. The low spatial resolution (1 meter) flight lines were the subject of this study.

As shown in Figure 18, only three of the 1 meter spatial resolution flight lines contained targets. These lines are 003_0320-1724, 004_0320-1706 and 005_0320-1700 and were the only lines processed any further.
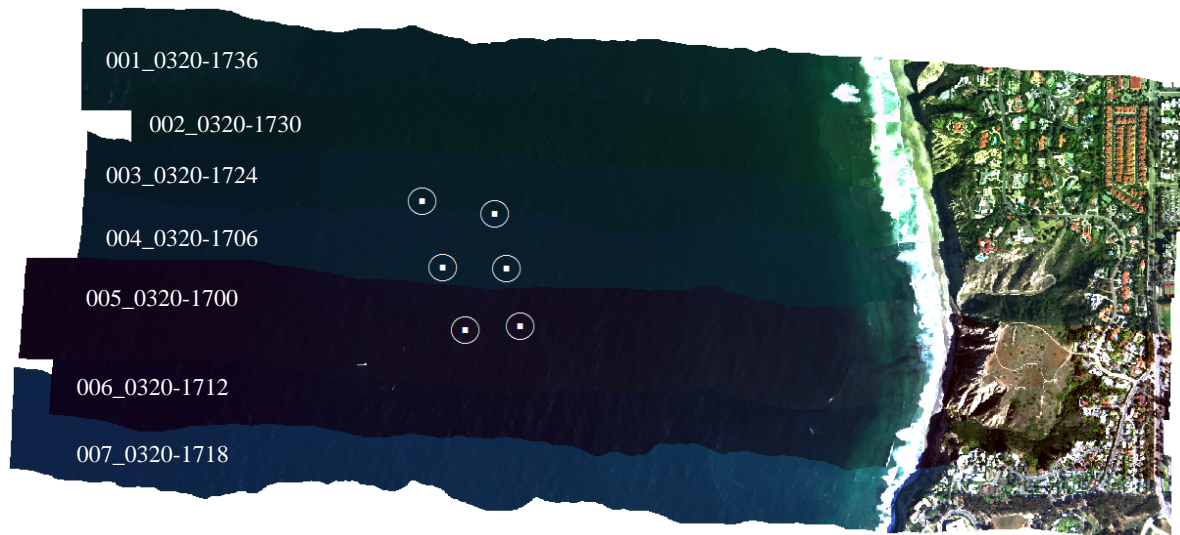
Figure 18.   1 meter spatial resolution, true color composite images (R: 641 nm, G: 551 nm, B: 460 nm), of the geocorrected flight lines overlaid by the known location of the targets

2.   Multiple Pixels

Prior to any spectral or image processing, each of the targets are visually identifiable in true-color composites of the data. As shown in Figure 19, the sub-pixel-

size targets appear to encompass multiple pixels in size. This is assumed to be due to the impulse response of the instrument (real electro-optical systems do not have point responses).
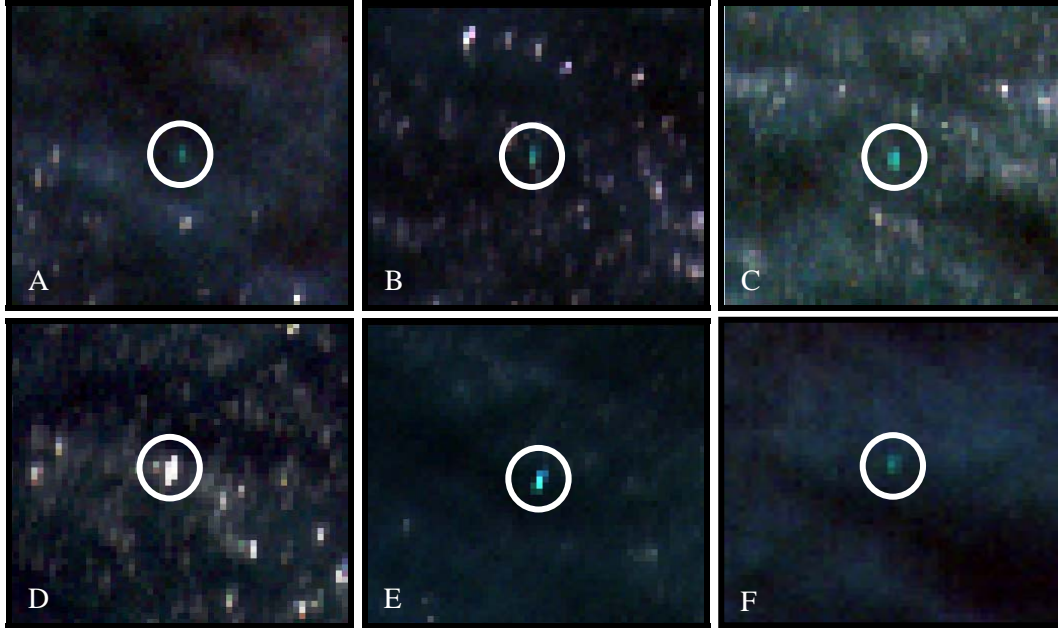
Figure 19.   The center pixels of each frame are the targets, which are the 3 (A), 2 (B) and 1 (C) meter submerged targets, the white surface target (D) the green surface target (E) and the black surface target (F). These sub-pixel size targets encompass between 4 and 8 pixels. Each frame is a 6 times magnification of a true color composite image (R: 641 nm, G: 551 nm, B: 460 nm) that has been linearly stretched

3.   Additional Scene Elements

The additional objects discussed in Chapter III are also visible in the scene. As Figure 20 shows, the yellow, orange, blue, green and black sub-meter diameter surface buoys, as well as the calibration experiment elements are visually identifiable in true color composites of the data.
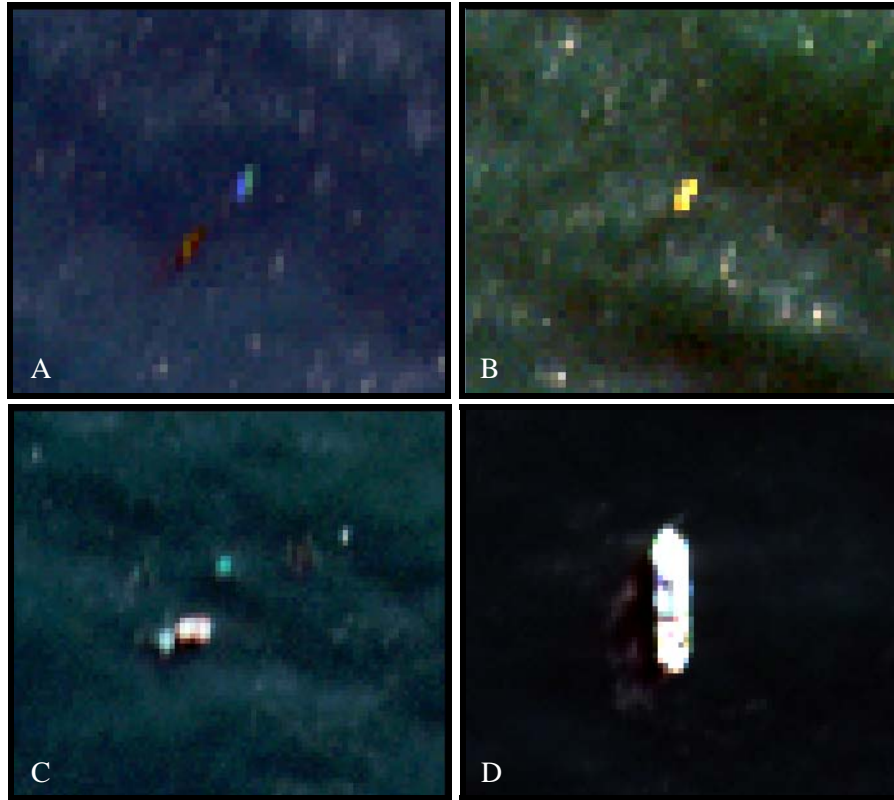
Figure 20.   The additional objects that are visually identifiable in the flight lines. Frame A shows the orange, black, blue and green surface buoys (in order from left to right), B shows the yellow surface buoy, C shows the four 2 x 2 meter calibration panels and 5.5 meter Zodiac, and D shows the 33.5 meter M/V Merlin. Each frame is a 4 times magnification of a true color composite image (R: 641 nm, G: 551 nm, B: 460 nm) that has been linearly stretched

C.   ANOMALY DETECTION PROCESS

Spectral unmixing is a technique that is sensitive to minute changes in the spectrum of a pixel. Retaining the spectral integrity of each pixel is of utmost importance. Atmospheric corrections, glint removal and other processing techniques may alter spectral characteristics (Vahtmae, 2008) and thus were avoided. Additionally, the stated purpose of this paper was to propose an operational method to quickly and accurately detect targets. As such, the least amount of processing steps necessary were used to complete the task.

As the target spectra were taken directly from the data, conversions to reflectance were unnecessary—both the target spectra and the data were in radiance. This technique would require the imaging of a known target during the time of collection in order to assure that the solar incidence angle, atmospheric parameters and solar source energy is similar. If this cannot be done, then both the target spectra and the scene have to be converted to reflectance values.

The flight paths for the data collection were planned at optimal solar geometries in order to avoid glint in the data. This was mostly successful and so glint removal from the images was not necessary.

1. Data Subset

a. *Spatial*

As the focus of this study was target detection in *non-littoral, deep waters*, the data was spatially subset prior to processing in order to remove the land and littoral areas. The new size of the three images was 2000 pixels long by 320 pixels wide.

b. *Spectral*

The first step in processing the data was to divide the target detection process into 2 distinct segments: detection of submerged targets and detection of surface targets. This allowed for the exploitation of the unique spectral characteristics of each target type. Due to the limited wavelength range that can penetrate into seawater effectively, the submerged target flight lines were spectrally subset to bands 3 through 46, covering 400 to 598 nm.

When searching for the surface targets, the determination was made to use all of the bands. However, after a visual inspection of the spectra throughout the image, an anomalous spike present in each pixel was located around band 123 (1,000 nm wavelength). As this is the spectral location of the overlap between the SWIR and VNIR

43

focal planes, this spike was determined to be a sensor artifact. Bands 115 through 150, covering 929 through 1149 nm were added to ENVI's bad band list, effectively removing them from the data.

2.   RX Anomaly Detection

In ENVI, a RXD-UTD Anomaly Detection algorithm was initially applied to the flight lines using all of the spectral bands and then subsequently reapplied to the same lines, sub-setting them to just the water penetrating bands discussed earlier. Rule images were output from the algorithm and the density slice function was used as a threshold to filter out the target pixels. As a logical initial threshold value, the brightest 2% of the pixels were selected. The threshold was then adjusted in order to isolate the targets.

3.   MTMF Anomaly Detection

a.   Sample Target Spectra

MTMF requires an input target spectrum and thus representative targets for the submerged and the surface targets were chosen. For the submerged targets, the 2 meter target was chosen and for the surface targets, the green target was chosen. In order to collect a spectrum from each target, a region of interest (ROI) was drawn covering the pixels the target encompassed (3 pixels for the 2 meter submerged target and 4 pixels for the green target). The mean spectrum of these ROIs was then calculated and recorded as an ASCII file. The same procedure was followed in order to calculate a non-target spectrum: a 69,000 pixel polygon ROI was created over a representative water region with small amounts of surface clutter and glint. The mean spectrum of the water was then used in the non-target section of the target detection wizard.

b.   Target Detection Wizard

As part of ENVI's spectral tools, the Target Detection Wizard guides the user through the process of finding targets in hyperspectral or multispectral data. The steps are as follows (Modified from ENVI Help, Version 4.8):

1. Input / Output File Selection

2. Atmospheric Correction (optional)

3. Target Spectra Selection

4. Non-Target Spectra Selection

5. MNF Transformation

6. Target Detection Methods

7. Rule Images and Results Preview

8. Target Filter

9. Export Results

10. View Statistics and Report

The first five steps of the wizard are self-explanatory or have been discussed previously. Step 6 of the wizard gives the user the option of a multitude of detection algorithms, including MTMF. In this study, MTMF was the only method chosen.

Step 7 outputs the MTMF Rule Image, as well as a full band scatter plot. Full band scatter plots compare a pixel's MF score (horizontal axis) to its infeasibility score (vertical axis). This plot is similar to an n-dimensional plot except it includes the values for the entire scene. The similar background (water) pixels form a data cloud with low infeasibility and MF scores, while the target pixels are outliers, generally with low infeasibility scores and high MF scores (e.g. good match to the target spectrum and a feasible mixture). Targets tend to project out from the data cloud like fingers, allowing for easy delineation. Pixels deemed as targets by the wizard are highlighted red. Additional pixels determined to be target pixels by the user were highlighted as well. Figures 21 and 22 show plots created for flight line 004 with the 2 meter submerged and surface targets, respectively. Note the circled outliers denoting the pixels deemed to contain the target.
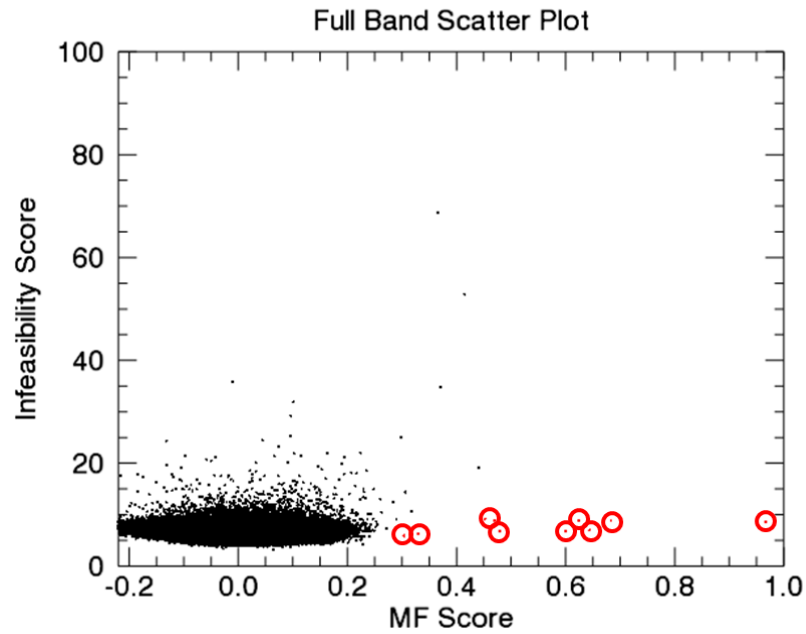
Figure 21.   Full band scatter plot showing the pixels deemed target pixels for the 2 meter submerged target. The horizontal axis is the MF score and the infeasibility score is the vertical axis. The circled pixels are the targets of interest and have high MF scores with low infeasibility values
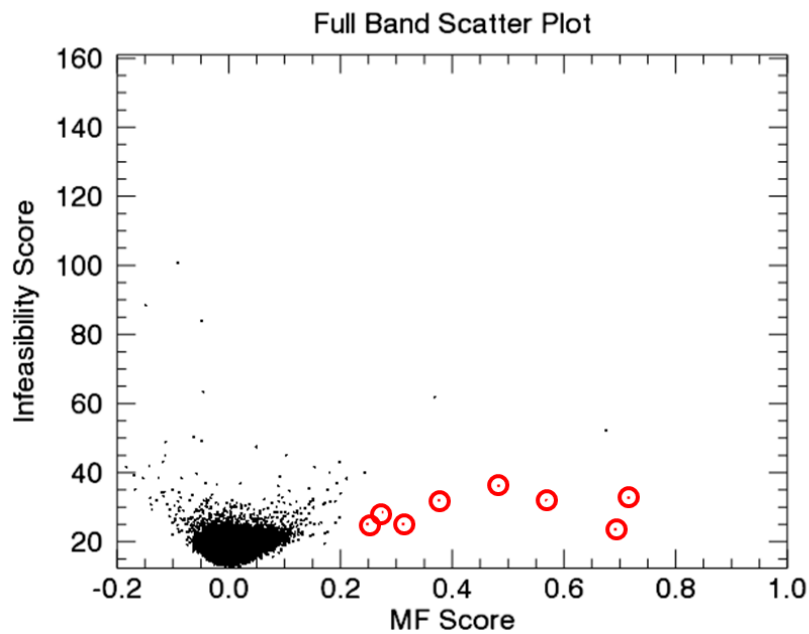
Figure 22.   A full band scatter plot showing the pixels deemed target pixels for the green surface target. The horizontal axis is the MF score and the infeasibility score is the vertical axis. The circled pixels are the targets of interest and have high MF scores and low infeasibility values

Step 8 allows for basic filtering options, including clumping and sieving. For both the surface and submerged targets, these settings were left as the recommended defaults, which include a clumping operator of 3 rows by 3 columns and a sieving parameter using 8 neighboring pixels.

With the last two steps of the target wizard, a target ROI was created and then overlaid on the true color image. The locations of the ROIs were then compared to the known locations of the targets to assess accuracy.

The spectrally subset versions of flight lines 003, 004 and 005 were run through this process individually, using the mean 2 meter submerged sample target spectrum as the input target (Step 3). This process was then duplicated using the non-spectrally subset versions of the flight lines and the mean green surface target sample spectrum as the input target (Step 3).

THIS PAGE INTENTIONALLY LEFT BLANK

V. RESULTS AND ANALYSIS

A. ANOMALY DETECTORS

When searching for targets in water, the primary complication is the small size and limited number of targets as compared to the amount of clutter (glint, ocean wave crests, etc.). This clutter tends to lead to high false alarm rates that can limit the usefulness of any anomaly detector. For example, with many typical remote sensing techniques, "it is common to have 100 false alarms due to clutter for every real mine present" (Williams, Myers, & Silvious, 2009, pp. 1). Thus when analyzing the usefulness of any anomaly detector, one should look at both its false negative *and* false positive results (Williams, et al., 2009).

1. RX Anomaly Detector

The RXD-UTD output is a rule image, with the values of each pixel representing the RXD-UTD score; the larger the score, the more anomalous the pixel. These results are shown in Figures 23 through 25. Each figure shows a section of the flight line that contains the targets in true color with a square root stretch, the submerged target results and the surface target results. This process lacks a default threshold or a way to isolate the targets (high values) from the false positives (low values). In order to compare the images a baseline was chosen, density slicing the images to show the brightest 2% of the pixels.
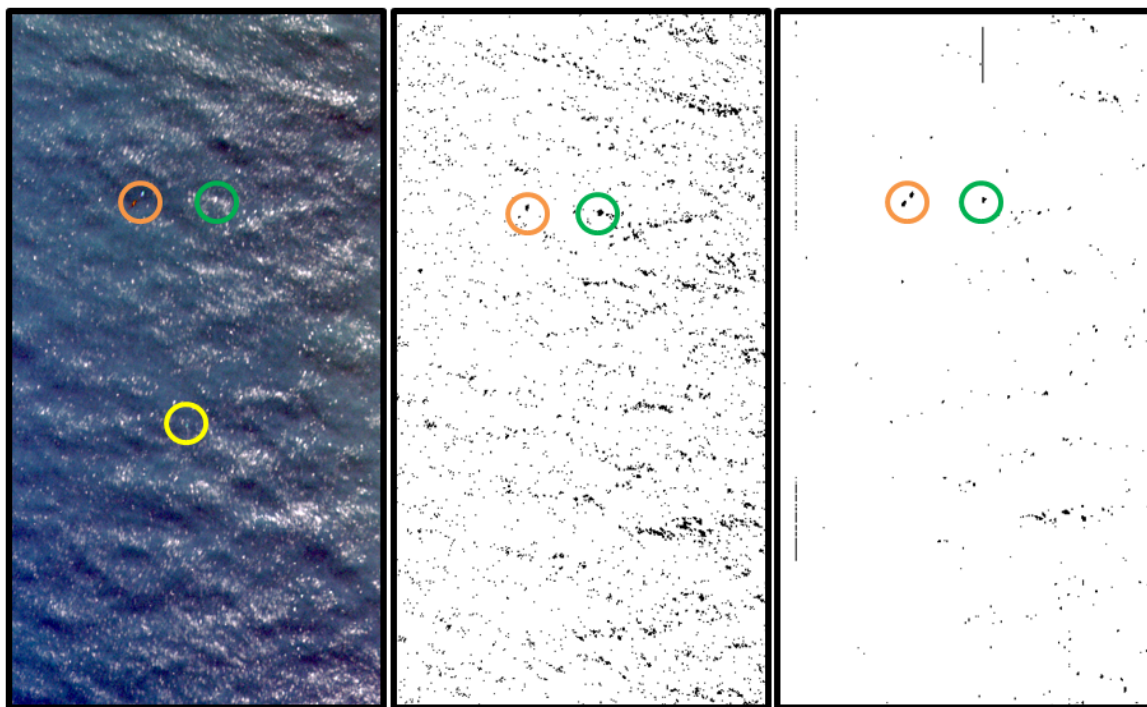
Figure 23.   Flight line 003 RXD-UTD results. The left image is a true color composite
(R: 641 nm, G: 551 nm, B: 460 nm), the center image is the submerged target
RXD-UTD result and the right image is the surface target RXD-UTD result. The
submerged target (yellow), surface target (green) and marker buoys (orange) are
circled
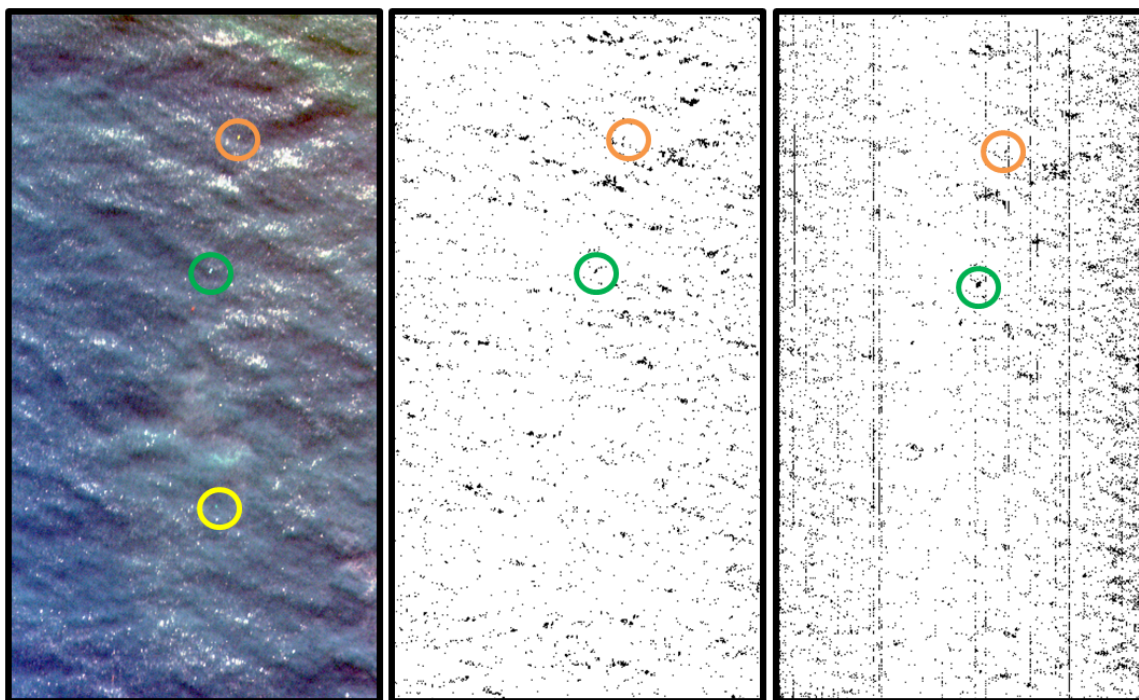
Figure 24. Flight line 004 RXD-UTD results. The left image is a true color composite (R: 641 nm, G: 551 nm, B: 460 nm), the center image is the submerged target RXD-UTD result and the right image is the surface target RXD-UTD result. The submerged target (yellow), surface target (green) and marker buoys (orange) are circled
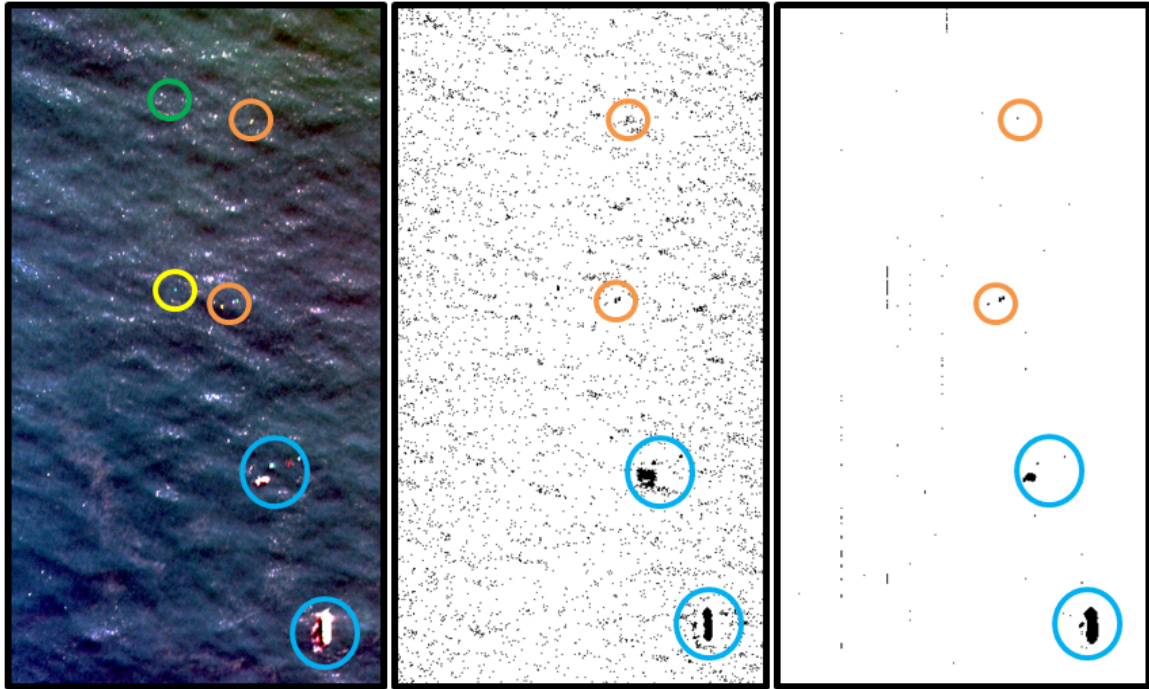
Figure 25. Flight line 005 RXD-UTD results. The left image is a true color composite (R: 641 nm, G: 551 nm, B: 460 nm), the center image is the submerged target RXD-UTD result and the right image is the surface target RXD-UTD result. The submerged target (yellow), surface target (green), marker buoys (orange) and calibration experiment elements (blue) are circled

With 0 true positive detections, the RXD-UTD algorithm did not detect the submerged targets or the black surface target. Further analysis was impossible without target pixels selected.

The RXD-UTD located the green and white surface targets. In order to evaluate the ability of the detector to locate the targets as compared to false alarms, the initial threshold value was set to the brightest 2% of the pixels and then was increased by 500 points at a time until the targets were no longer selected.

Each pixel identified as a target by the algorithm was counted as either a true positive (TP) or a false positive (FP). Due to the pixel "blurring" effect previously discussed, pixels immediately adjacent to the target pixels were not deemed false positives if selected. The previously discussed field testing elements, including the calibration panels and the M/V Merlin were counted as false positives when identified by

52

the anomaly detectors. If an analysis intended to locate surface targets selected pixels containing a submerged target (or vice versa), this was considered a favorable result and deemed a true positive. If a pixel identified prior to the wizard as a target pixel was not identified by the wizard, it was counted as a false negative (FN). Any pixel in the image that did not contain a target and was not selected by the wizard was deemed a true negative (TN).

A common technique to evaluate the performance of a detection algorithm is to calculate the true positive rate (TPR) and the false positive rate (FPR):

$$TPR = \frac{TP}{TP + FN} \qquad\qquad 5.1$$

$$FPR = \frac{FP}{FP + TN} \qquad\qquad 5.2$$

Table 2 lists the results of this analysis.

Table 2.   Pixel-based RXD-UTD results, along with threshold

Type	Line #	Target	Threshold Value (RXD-UTD Score)	TP	FP	FN	TN	TPR	FPR
Surface	003	White	786	13	16504	0	623483	1.00	2.6E-02
			1286	8	529	0	639463	1.00	8.3E-04
			1786	8	202	0	639790	1.00	3.2E-04
			2286	8	102	0	639890	1.00	1.6E-04
			2786	7	58	0	639935	1.00	9.1E-05
			3286	7	42	0	639951	1.00	6.6E-05
			3786	5	33	0	639962	1.00	5.2E-05
			4286	5	30	0	639965	1.00	4.7E-05
			4786	4	27	0	639969	1.00	4.2E-05
			5286	4	23	0	639973	1.00	3.6E-05
			5786	3	19	1	639977	0.75	3.0E-05
			6286	2	17	2	639979	0.50	2.7E-05
			6786	2	16	2	639980	0.50	2.5E-05
			7286	2	15	2	639981	0.50	2.3E-05
			7786	2	15	2	639981	0.50	2.3E-05
			8286	1	14	3	639982	0.25	2.2E-05
			14286	0	5	4	639991	0.00	7.8E-06
Surface	004	Green	421	19	23341	0	616640	1.00	3.6E-02
			921	8	71	0	639921	1.00	1.1E-04
			1421	7	20	1	639972	0.88	3.1E-05
			1921	5	10	2	639983	0.71	1.6E-05
			2421	4	5	4	639987	0.50	7.8E-06
			2921	3	4	5	639988	0.38	6.3E-06
			3421	3	3	5	639989	0.38	4.7E-06
			3921	2	3	6	639989	0.25	4.7E-06
			4421	2	3	6	639989	0.25	4.7E-06
			4921	2	3	6	639989	0.25	4.7E-06
			5421	2	3	6	639989	0.25	4.7E-06
			5921	2	3	6	639989	0.25	4.7E-06
			6421	2	3	6	639989	0.25	4.7E-06
			6921	1	2	7	639990	0.13	3.1E-06
			13421	0	0	0	640000	0.00	0.0E+00

A variant of a typical receiver operator characteristics (ROC) curve was then created by plotting the TPR and FPR against the threshold value. As Figures 26 and 27 show, this technique allows for a side-by-side comparison of the curves. By plotting the threshold values on the horizontal axis, it allows threshold values to be evaluated with

regard to FPRs and TPRs. Note the different scale of each of the two horizontal axes. In order to better visualize the small values in the large range of the FPR, this axis was set to a logarithmic scale.
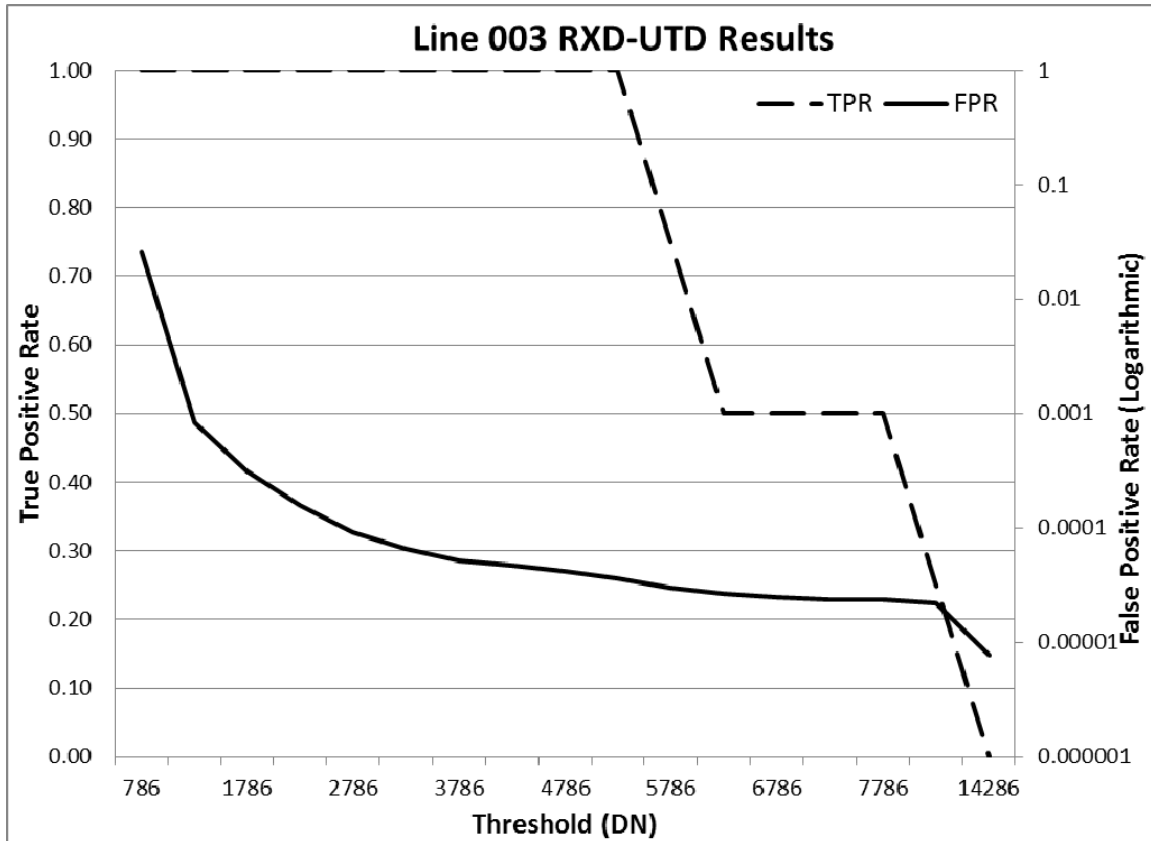
Figure 26.   Flight line 003 variant ROC curve evaluating the RXD-UTD results. The left vertical axis is the true positive rate and the right vertical axis is the false positive rate. Note the different scales between the vertical axes. The right vertical axis has a logarithmic scale in order to better visualize small values. The horizontal axis is the threshold DN
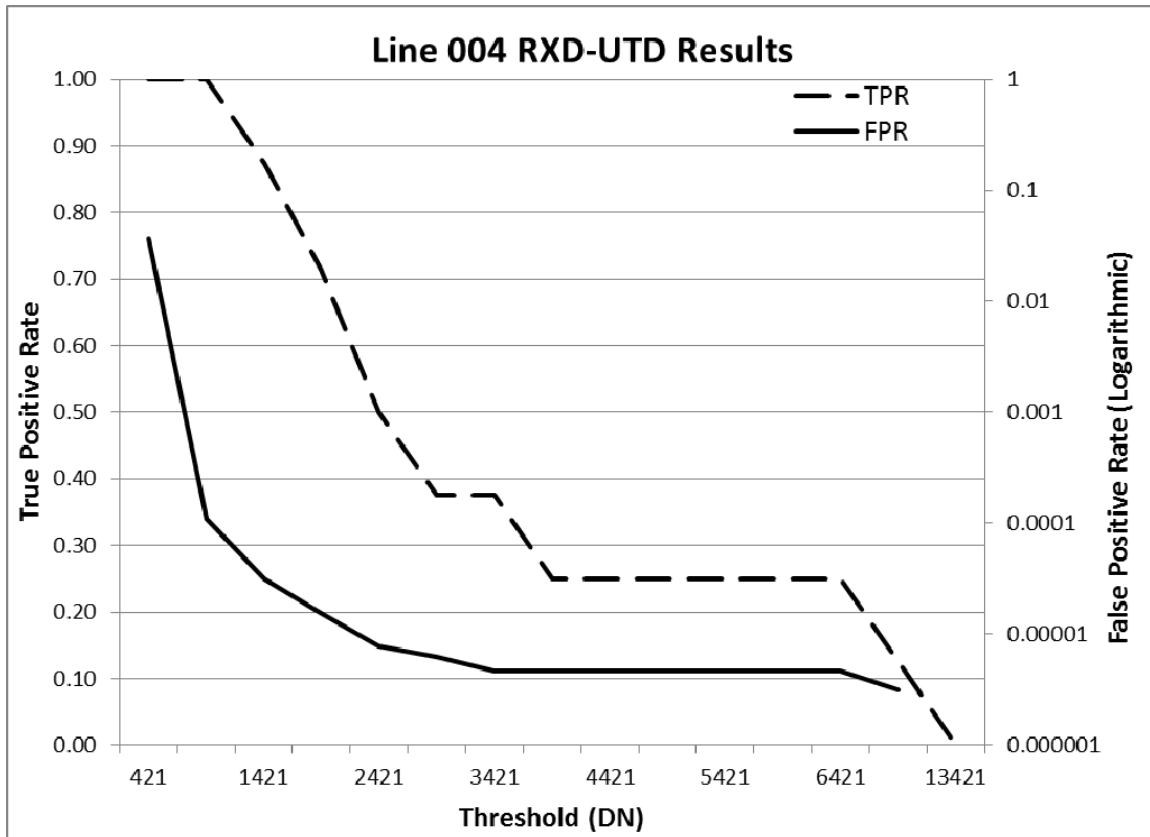
Figure 27.   Flight line 004 variant ROC curve evaluating the RXD-UTD results. The left vertical axis is the true positive rate and the right vertical axis is the false positive rate. Note the different scales between the vertical axes. The right vertical axis has a logarithmic scale in order to better visualize small values. The horizontal axis is the threshold DN

Table 2 and the variant ROC curves in Figures 26 and 27 illustrate the relative effectiveness of using a RX-UTD algorithm with 1 meter hyperspectral data to detect sub-pixel surface targets. For line 003, the algorithm is able to detect targets at a 100% true positive rate with a 0.003% false positive rate. The results are similar when line 004 is run through the process, with an 88% true positive rate at a 0.003% false positive rate.

Another useful way to evaluate the process is to look at the clumped pixels as single objects instead of evaluating individual pixels. This means each target is one object, regardless of the number of pixels it encompasses. As the true number of "objects" in an image is undefined (everything from a single pixel of glint to the M/V Merlin can be an "object"), this technique prevents the calculation of a true negative

value and thus an FPR. However, an object-based result is easier to conceptualize. Pixels clumped together were counted as one object. A single selected pixel of a target was counted as 100% detection, even if the target encompassed multiple pixels. As before, if an analysis intended to locate surface targets selected a pixel containing a submerged target (or vice versa), it was not counted as a false positive. The largest threshold that still identified the target was used, as this also allowed the least number of false positives. As the submerged targets were not identified, regardless of threshold value, nor were the targets in line 005, these results are not provided. The remaining results are shown in Table 3.

Table 3.   Object-based RXD-UTD results, along with the threshold values and descriptions of the objects identified

Type	Line #	Target	Threshold Value (RXD-UTD Score)	Target Detection %	# of False Postives	Notes
Surface	003	White	8286	100%	4	surface target, yellow buoy and 3 patches of glint identified
Surface	004	Green	6921	100%	1	surface target and a single patch of glint identified

a.   Further Analysis

This seemingly positive result must be examined further. The process failed to locate targets in 4 of the 6 lines. Neither the submerged targets, nor the black surface target were found. These targets are the most difficult to discern from a background, but also the most realistic type of targets. The failure of this technique in these situations cannot be overlooked.

Although the experiment returned low false positive rates with high true positive rates, the values were calculated with regards to number of pixels. High spatial resolution HSI images covering large surface areas have an extremely large number of pixels. This means the low false positive rates would equate to a large number of false positives. For instance, applying the 100% true positive rate and 0.0036% false positive rate to just the three flight lines used in this experiment, covering 1,920,000 square meters (1,920,000 pixels) equates to 69 false alarms. That number of falsely identified

pixels is relatively high when compared to the 6 targets that were placed in the area, covering less than 25 pixels. To put this into context, Bab-el-Mandeb, the narrow straight at the mouth of the Red Sea, which was mined in 1984, covers about 5,200,000 square meters. In order to detect 100% of the mines throughout this area, with the RXD-UTD false positive rates listed previously would detect up to 187 false pixels. Even with a 75% target detection rate and 0.0029% false positive rate, the test would produce 154 false positive pixels.

When looking at the object-based analysis, a single pixel of the target can be found with much lower false alarm rates. In the case of line 004, only 5 objects were detected: 4 false alarms and the target. Line 005 had even better success, with only 2 objects detected: the target and 1 false alarm. This counting method is dependent on the clumping of pixels, however. If there are 154 false positive pixels and none of them are clumped, then the false alarm rate increases drastically.

2.   MTMF Results

Figures 28 through 30 show a section of the MTMF Target Detection Wizard rule images for flight lines 003, 004 and 005, respectively. The left images are true color composites (R: 641 nm, G: 551 nm, B: 460 nm), enhanced with a square root stretch in order to make the targets easier to view. The middle images are the submerged target rule images and the right images are the surface target rule images. The objects in each image have been circled with the following color code: the submerged targets are yellow, the surface targets are green, the marker buoys (non-targets) are orange, and the M/V Merlin and other calibration test elements (non-targets) are blue.
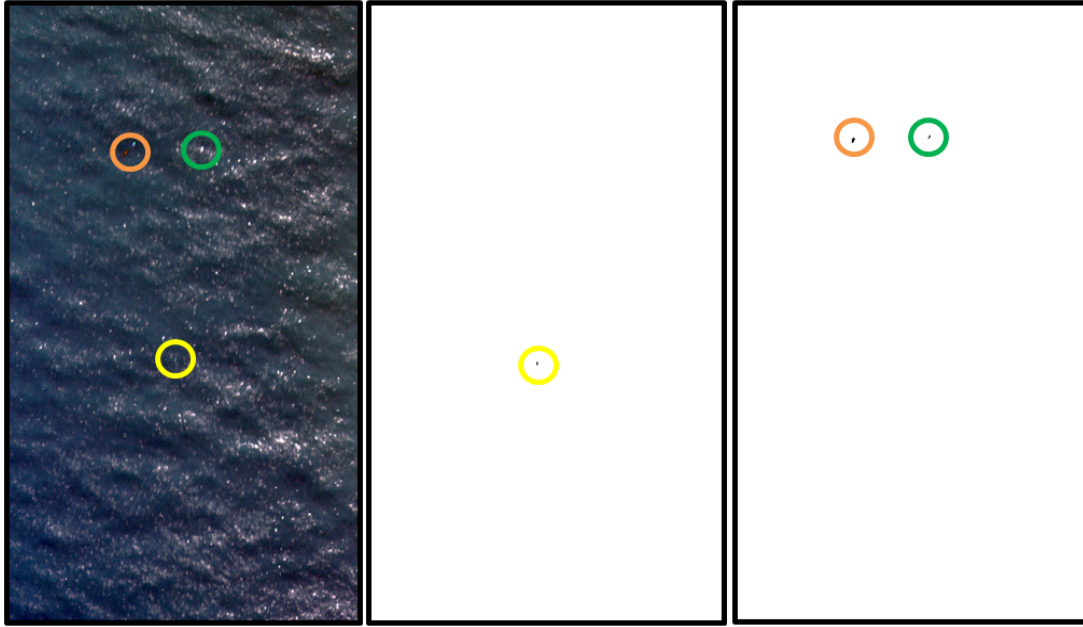
Figure 28.   Flight line 003 MTMF results. The left image is a true color composite (R: 641 nm, G: 551 nm, B: 460 nm), the center image is the submerged target MTMF result and the right image is the surface target MTMF result. The submerged target (yellow), surface target (green) and marker buoys (orange) are circled
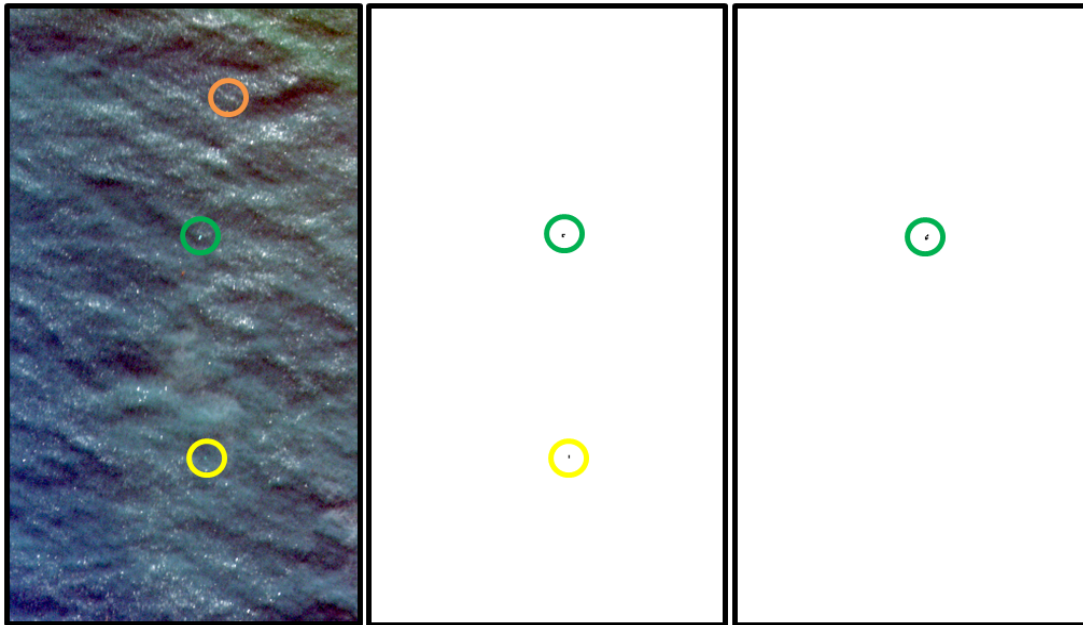
Figure 29.   Flight line 004 MTMF results. The left image is a true color composite (R: 641 nm, G: 551 nm, B: 460 nm), the center image is the submerged target MTMF result and the right image is the surface target MTMF result. The submerged target (yellow), surface target (green) and the marker buoys (orange) are circled
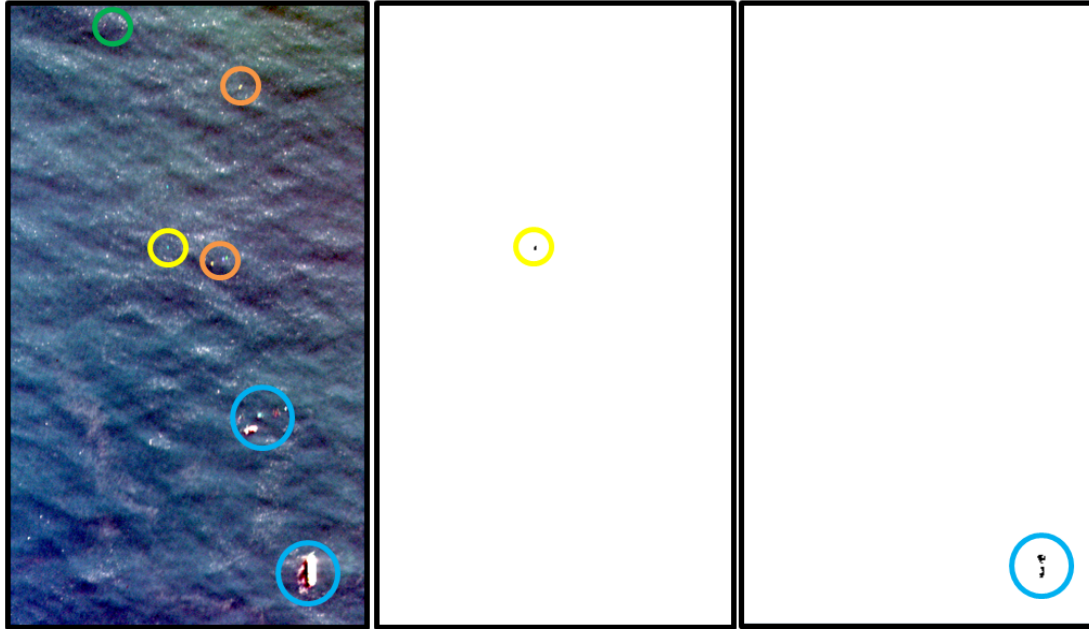
Figure 30.   Flight line 005 MTMF results. The left image is a true color composite (R: 641 nm, G: 551 nm, B: 460 nm), the center image is the submerged target MTMF result and the right image is the surface target MTMF result. The submerged target (yellow), surface target (green), the marker buoys (orange) and the calibration experiment elements (blue) are circled

Table 4 lists the pixel-based results of the MTMF Target Detection Wizard analysis. The same pixel-counting rules defined in the RXD-UTD results (regarding TP, TN, FP and FN) were applied to this data set. Without a threshold value to adjust, TPRs, FPRs, and ROC curves are ambiguous and thus not are provided.

Table 4.   Pixel-based results of the MTMF Target Detection Wizard

Type	Line #	Target	TP	FP	FN	TN
Sub-merged	003	-2 m	3	0	0	639997
	004	-3 m	9	0	0	639991
	005	-1 m	5	0	0	639995
Surface	003	White	4	8	0	639988
	004	Green	9	0	0	639991
	005	Black	0	61	3	639936

For the submerged target MTMF analysis, the detector located the submerged target in each flight line with no false positives. In flight line 004, the wizard detected both the submerged target and the surface target.

For the surface target MTMF analysis, the detector located the white and green surface targets in lines 003 and 004, respectively, but not the black surface target in line 005. With line 003, the only false positives were the 8 pixels of a yellow marker buoy. The 0 false positives and 0 false negatives for line 004 is slightly deceptive, as this is the line the average green surface target spectrum was taken from. In line 005, the detector falsely identified the M/V Merlin and a few pixels of glint as a target, but was unable to locate the black surface target. None of the surface MTMF analyses located the submerged targets.

The same object-based analysis that was detailed in the RXD-UTD section was performed on the results. Table 5 shows these descriptions.

Table 5. Object-based MTMF results, along with descriptions of the objects identified

Type	Line #	Target	Target Detection %	# of False Positives	Notes
Sub-merged	003	-2 m	100%	0	submerged target only object identified
	004	-3 m	100%	0	submerged and surface target identified
	005	-1 m	100%	0	submerged target only object identified
Surface	003	White	100%	1	surface target and a yellow marker buoy identified
	004	Green	100%	0	surface target only object identified
	005	Black	0%	2	M/V Merlin and ocean clutter identified

a. *Further Analysis*

(1) Error Analysis. The most critical step in a MTMF target detection process is differentiating between target pixels and background pixels in the full scene scatter plot. If the target spectrum is not unique enough from the background, its

pixels are lost in the data cloud. This is the primary reason the submerged targets were successfully found—they are easily distinguished from the background data cloud (this is shown in Figure 21). As Figure 31 shows, a large, highly reflective object can overpower a scatter plot, making target pixel delineation impossible. This scatter plot is from the non-spectrally subset flight line 005, which appears to have sensor noise and includes the M/V Merlin, the calibration experiment elements, marker buoys and both the 1 meter submerged and black surface targets. Operationally, large, highly reflective objects should be masked out prior to MTMF analysis.
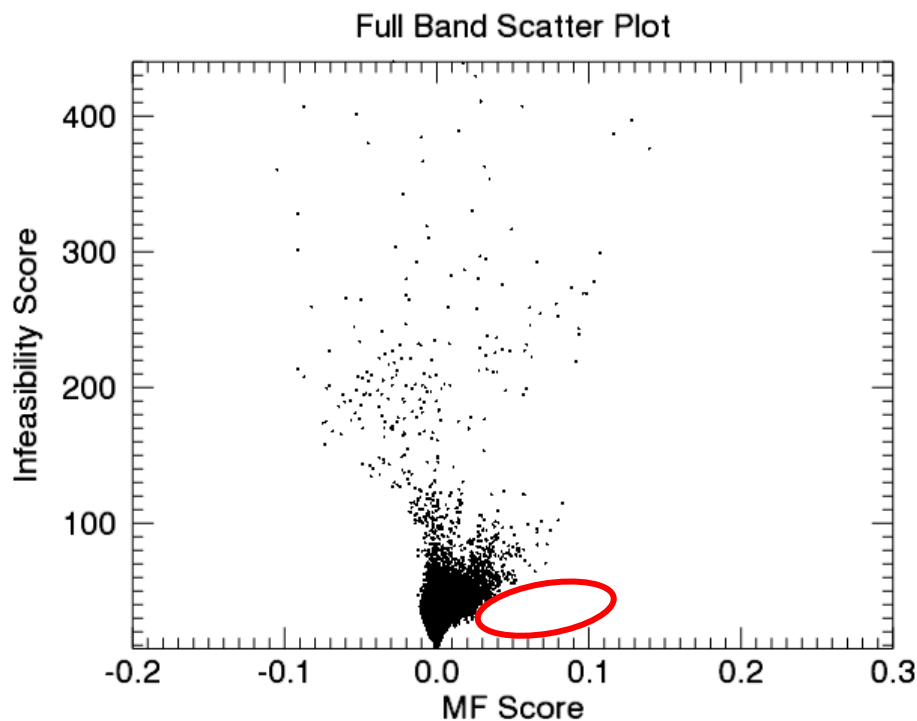
Figure 31.   Flight line 005 full band scatter plot when run through the surface target MTMF detection wizard. This plot has a different horizontal and vertical scale than the previous full band scatter plots. Note the lack of outlier pixels with low infeasibility score and high MF scores (the red circle). This mean the targets cannot be isolated in this plot

b.   *Verification*

Due to the extreme success of this process, additional verification tests were run to look for potential biases.   These test involved repeating the process, introducing a new variable each time.

(1) Other Input Targets.   The wizard was run using the black surface target and the 3 meter submerged target as the input sample targets, replacing the green surface target and the 2 meter submerged target, respectfully.   These results were similar to the results listed in the text above.

(2) Littoral Zones. This process was then duplicated using a larger spatial subset, leaving the littoral zones in the overall scene.   This had the effect of introducing a large amount of clutter into the scene.   The initial results to this test were promising, although without a relatively homogenous background, the target pixels are harder to discern in the full scene scatter plots.   This resulted in a much higher false positive rate.

(3) Other Flight Lines. A pivotal experiment, testing the response of the wizard when no targets were present, was run using the flight lines that were known to not contain targets. The same process described in the text above was used. The results are displayed in Table 6. There were 0 TPs for all of the tests as no targets existed. The submerged target analyses resulted in 2 to 4 false positive pixels. The false positives in lines 002 and 006 were due to the blue surface buoys that were in the frame. The 2 false positive pixels in line 007 were due to glint. The surface MTMF analyses returned 2 false positive pixels in line 002 as a result of the blue surface buoy. Neither line 006 nor 007 had a false positive.

Table 6.   Pixel-based MTMF results of the flight lines not containing targets

Type	Line #	Target	TP	FP	FN	TN
Sub-merged	002	N/A	0	2	0	639998
	006	N/A	0	4	0	639996
	007	N/A	0	2	0	639998
Surface	002	N/A	0	2	0	639998
	006	N/A	0	0	0	640000
	007	N/A	0	0	0	640000

B.   SPECTRAL OR SPATIAL?

The results above, especially the MTMF analysis outpaces the results from similar work done at this test range.   Using 2.2 meter spatial resolution WorldView-2 multispectral data, Sandersfeld (2012) was able to identify the targets using a combination of principle component analysis and a RXD-UTD algorithm, but had false alarm rates greater than 20%. With both a lower spectral and spatial resolution than the ProSpecTIR-VS3 data, Sandersfeld's results beg the question: "Were the higher detection rates and lower false positive rates of the MTMF analysis due to the higher spatial or spectral resolution?"

1.   Spatial Analysis

In order to evaluate the contributions of spatial resolution to the success of the anomaly detector two additional tests were run. The 1 meter resolution data were subsampled by a factor of 0.5, essentially decreasing the number of pixels by 50%. The resulting lines featured the same spectral resolution as the previous data in this study, but had a lower spatial resolution, similar to WorldView-2. These newly created 2 meter spatial resolution lines were put through the process detailed previously. Due to the decrease in number of pixels, the pre-analysis spatial subset differed from that listed previously. In this experiment the lines were spatially subset to 160 x 1000 pixels. The pre-analysis spectral subsets were left the same, using bands 3 through 46 for the submerged targets and all of the bands for the surface targets. The pixel-based results of the MTMF analysis are shown in Table 7.

Table 7.   Pixel-based results of the MTMF Target Detection Wizard, using the 2 meter spatial resolution data

Type	Line #	Target	TP	FP	FN	TN
Sub-merged	003	-2 m	2	0	0	159998
	004	-3 m	4	0	0	159996
	005	-1 m	3	7	0	159990
Surface	003	White	3	3	0	159994
	004	Green	4	0	0	159996
	005	Black	0	22	0	159978

The 2 meter spatial resolution MTMF analysis technique had similar success to the previous 1 meter experiment, but with higher false positive rates. The line 003 and 004 submerged analysis detected the 2 meter and 3 meter submerged targets, respectively and had no false positives or false negatives. The analysis run on line 004 located both the green surface target and the 3 meter submerged target. The submerged MTMF analysis run on line 005 located the 1 meter submerged target, but also had 7 false positives: 3 pixels were the M/V Merlin and 4 pixels were the marker buoys. The surface MTMF analysis run on line 003 located the white surface target, but also had 3 false positives on glint. With line 005, the surface analysis had a lack of success detecting the black surface target, with 22 false positive pixels (16 on the M/V Merlin, 6 on glint).

This same experiment was then repeated with the low altitude flight lines, featuring the same spectral resolution, but a higher spatial resolution (0.5 meters). The new spatial subset was 320 x 3500 pixels. This increase in spatial resolution resulted in the targets being larger than a pixel in size. Flight lines 006_0321-1655, 009_0321-1636 and 012_0321-1618 from March 21, 2012 of the low altitude data were used. The pixel-based results of the MTMF analysis are shown in Table 8.

Table 8.   Pixel-based results of the MTMF Target Detection Wizard, using the data with 0.5 meter spatial resolution

Type	Line #	Target	TP	FP	FN	TN
Sub-merged	006	-2 m	12	0	0	1119988
	009	-3 m	17	0	0	1119983
	012	-1 m	9	0	0	1119991
Surface	006	White	14	0	0	1119986
	009	Green	7	0	0	1119993
	012	Black	4	26	2	1119968

The results show an increase in accuracy of the detector, as only the surface target analysis of line 012 recorded a false positive and failed to identify a target. In this case the detector missed two pixels of the black surface target and falsely selected 26 pixels of the surface buoys. 3 of the pixels selected were actually the 1 meter submerged target (counted as a true positive). With the submerged target analysis, flight line 009 detected 11 pixels of the 3 meter submerged target and 6 pixels of the green surface target. For the surface target analysis of line 006, 8 pixels of the white surface target were selected and 6 pixels of the 2 meter submerged target were selected.

The change in spatial resolution appears to have an effect on the ability of the MTMF analysis to detect targets, but with the limited sample size, the magnitude of this effect is hard to estimate. With a lower spatial resolution, the targets that were detected previously were still detected, albeit with higher false positive rates. The higher spatial resolution allowed for the false positive rate to decrease and for the detection of the black surface target.

2.   Spectral Analysis

Figure 32 shows a comparison between spectral means of the 2 meter submerged target and water. The vertical axis is the digital number (DN) of the pixel and the horizontal axis is wavelength in nanometers. Note the similarities between the curves. In fact, little difference can be found between the spectra.
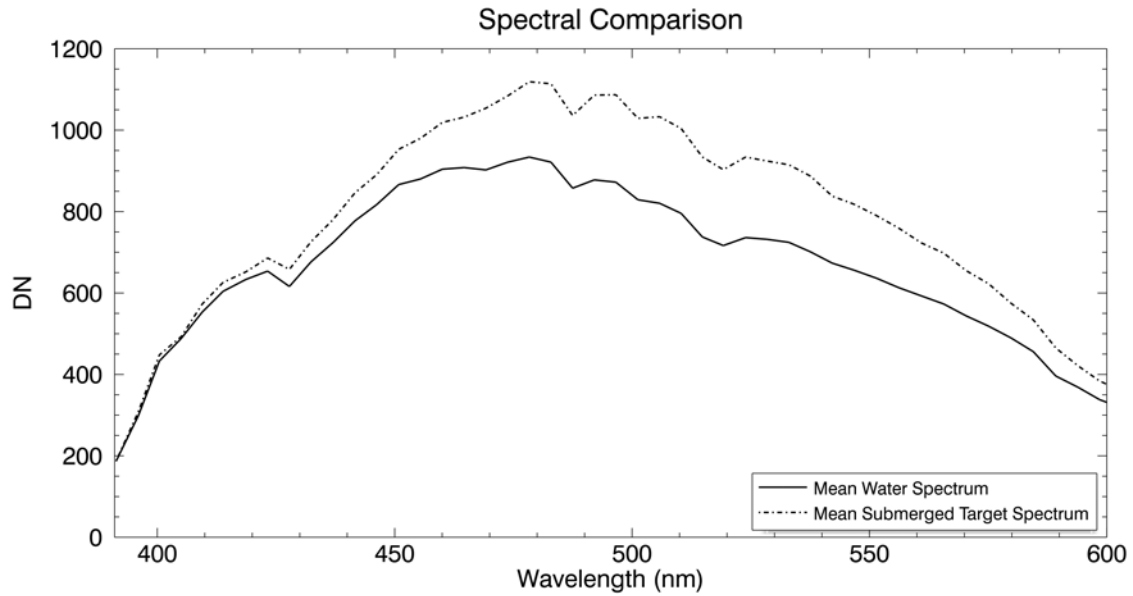
Figure 32.   Comparison between the spectral means of the 2 meter submerged target water. The horizontal axis is wavelength in nanometers and the vertical axis is the DN

Figure 33 compares the mean spectra of the green surface target and water. In this plot the green surface target spectrum appears to have a larger peak at 875 nm and a new absorption feature at 1390 nm. The gap between 929 and 1149 nm is due to the removal of bands containing sensor artifacts.
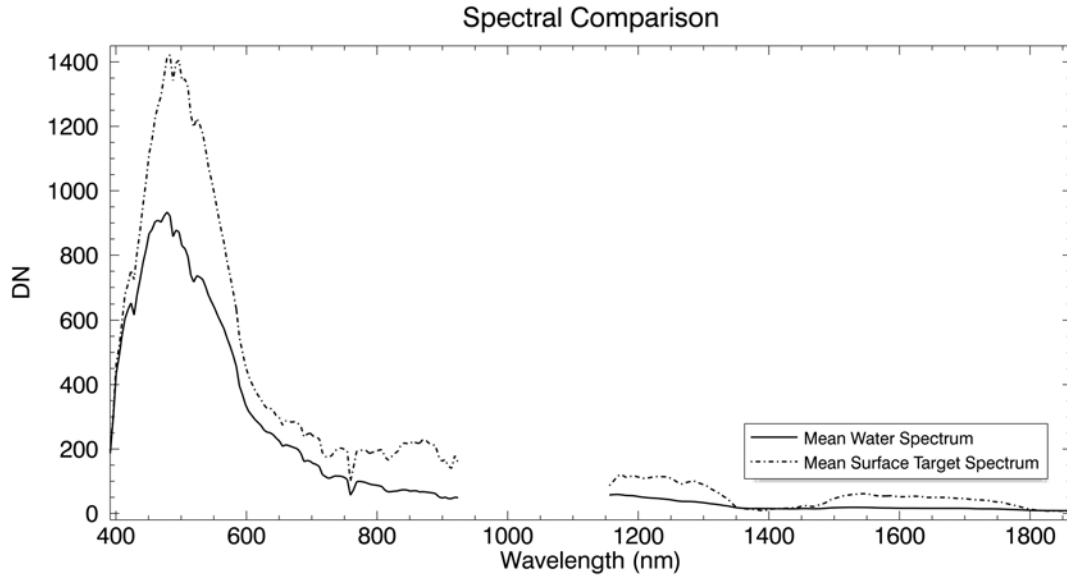
Figure 33.   Comparison between the spectral means of the green surface target and water.
The horizontal axis is wavelength in nanometers and the vertical axis is the DN.
The gap between 929 and 1149 nm is due to the removal of bands containing
sensor artifacts

In order to further examine the spectral differences, the mean target spectra were divided by the mean water spectrum, essentially normalizing the results and creating a difference curve. As Figure 34 shows, this technique allows for closer examination of the differences between the spectra. The difference curve for the submerged target spectrum shows absorption features at 405, 418, 487, 501, 519, 542, and 560 nm. These features are not vastly different than the mean water spectrum, with the deepest feature being only a few hundreds of a DN value. For comparison, the DN values in line 004 range from 205 to 6808. The continuum of the curve shows a slightly higher rise than the mean water spectrum.
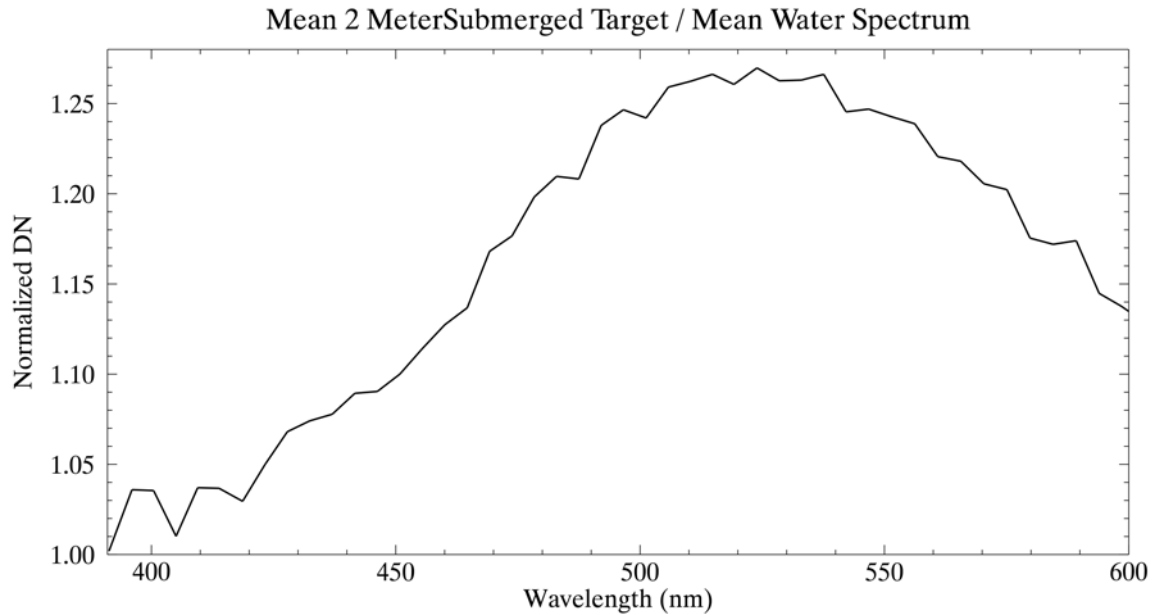
Figure 34.   Mean 2 meter submerged target spectrum normalized against the mean water spectrum. The horizontal axis is wavelength in nanometers and the vertical axis is a normalized DN

Figure 35, the difference curve for the mean green surface target, shows deeper absorption bands at 636, 1267, 1393, 2006, 2063 and 2452 nm, as well as new peaks at 514, 875, 1286, 1550 and 2100 nm. The gap between 929 and 1149 nm is due to the removal of bands containing sensor artifacts. The maximum magnitude of a difference feature is 2.65, compared to the image DN range of 6603.
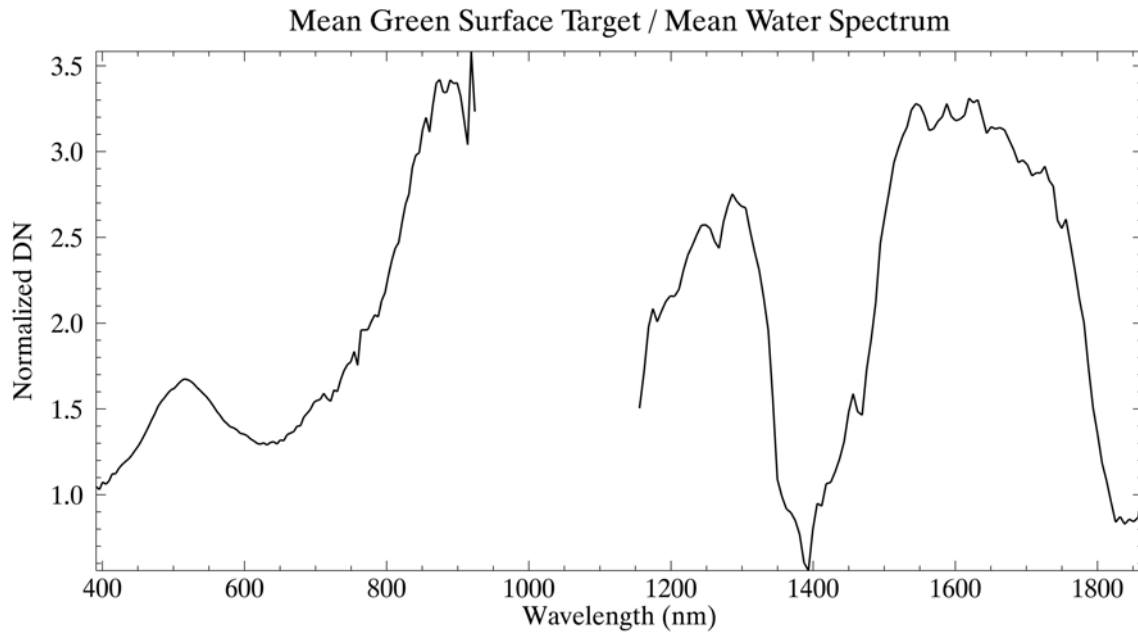
Figure 35.   Mean green surface target spectrum normalized against the mean water spectrum. The horizontal axis is wavelength in nanometers and the vertical axis is a normalized DN. The gap between 929 and 1149 nm is due to the removal of bands containing sensor artifacts

3.   Principle Component Analysis

Principle component analysis (PCA), the basis of the MNF transformation, allows for the examination of the dimensionality of spectral data. The first band of a principle component (PC) image is the average intensity of all of the bands. The subsequent bands give a quantitative value to the amount of spectral information in each pixel. By plotting the first band against a subsequent band in a scatter plot, one can analyze the amount of spectral information in each pixel (Olsen, 2007).

A PCA using covariance values was run on lines 003, 004 and 005 and then the first two bands of each PC image were plotted against each other in scatter plots. Figures 36 through 38 show these scatter plots, with the absolute values of PC band 1 on the horizontal axis and PC band 2 on the vertical axis. The absolute values of PC band 1 were used in order to visually clarify the plot. Separation of pixels in the vertical direction implies spectral differences, while horizontal separation implies intensity

differences. The data cloud contains the water pixels and the unmarked outliers are generally glint. The circled pixels are the submerged targets (green), surface targets (blue) and buoys (red).
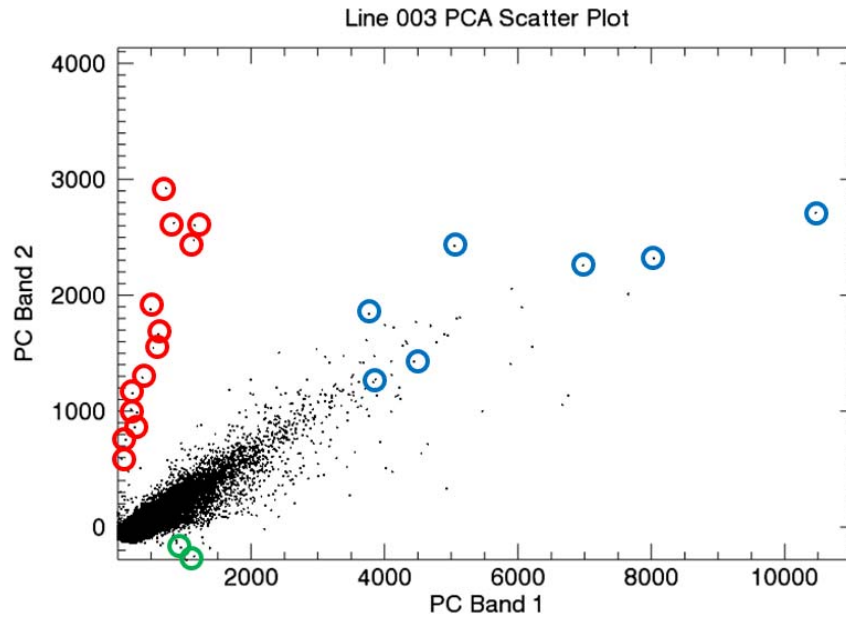
Figure 36. Scatter plot of the absolute values of PC band 1 (horizontal) versus PC band 2 (vertical) for line 003. The submerged target (green), surface target (blue) and buoys (red) are circled
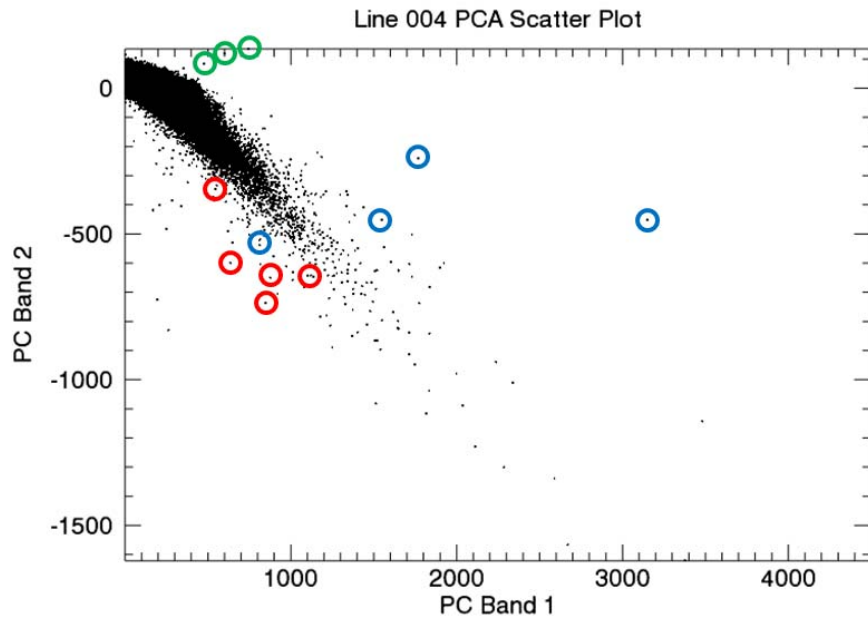
Figure 37.   Scatter plot of the absolute values of PC band 1 (horizontal) versus PC band 2 (vertical) for line 004. The submerged target (green), surface target (blue) and buoys (red) are circled
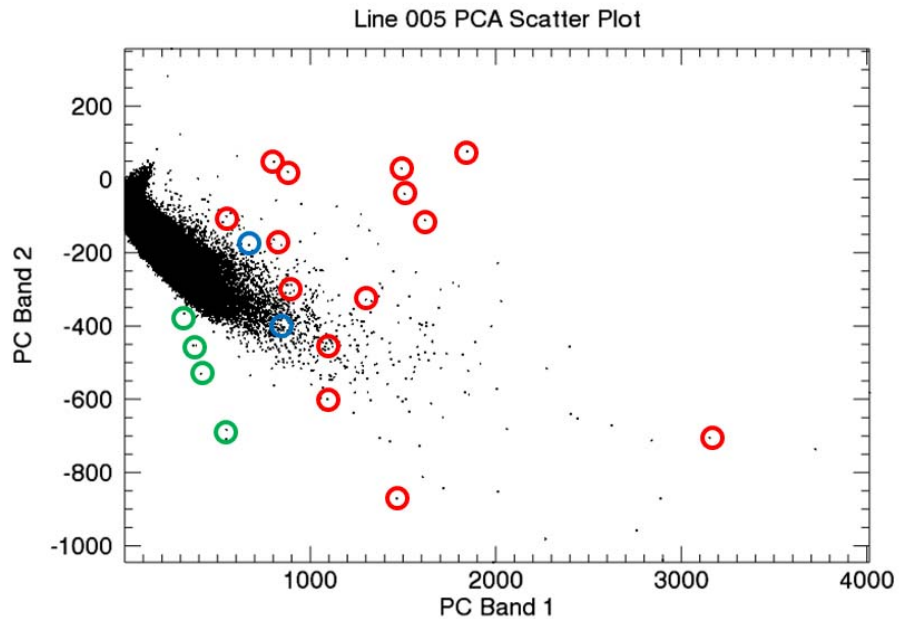
Figure 38.   Scatter plot of the absolute values of PC band 1 (horizontal) versus PC band 2 (vertical) for line 005. The submerged target (green), surface target (blue) and buoys (red) are circled

The ability of the MTMF analysis to spectrally detect the submerged targets with 100% true positive rates and 0% false positive rates is partially explained by the location of the submerged pixels in each of the scatter plots. Although the target pixels and the data cloud lie in a similar horizontal position, there is a distinct vertical separation. This means the submerged targets have intensities similar to the background water, but are distinct spectrally.

The less robust results of the MTMF analysis on the surface targets are explained by the intermixing of the surface target pixels with the glint (Figure 36), the buoys (Figure 37 and 38) or the water (Figure 38). The white surface target in line 003 has little spectral separation from the water, but can be differentiated due to its greater intensity values. Compared to the water, the green surface target in line 004 differs spectrally and in intensity. The black surface target in line 005, a particularly difficult target to detect, is spectrally similar to the water and differs in intensity only slightly, with little horizontal or vertical separation.

It should be noted, however, that it is unclear how the bands containing sensor artifacts impacted the calculation of the principle components. The eigenvalues of these bands were initially listed in the PCA results. When these bands were deleted from the data and then the PCA was rerun, the results appeared identical to the original results.

A line plot containing the values from the PCA of line 003 was created, using the eigenvalues of both PC band 1 and PC band 2 as the vertical axis and wavelength as the horizontal axis. This allowed for further analysis of the results above. Figure 39 shows this graph. The blue line is PC band 1 eigenvalues and the red dots are PC band 2 eigenvalues. The gap around 1000 nm is due to the removal of bands containing sensor artifacts. The horizontal axis range was cut at 1800 nm as nothing of note existed at longer wavelengths.
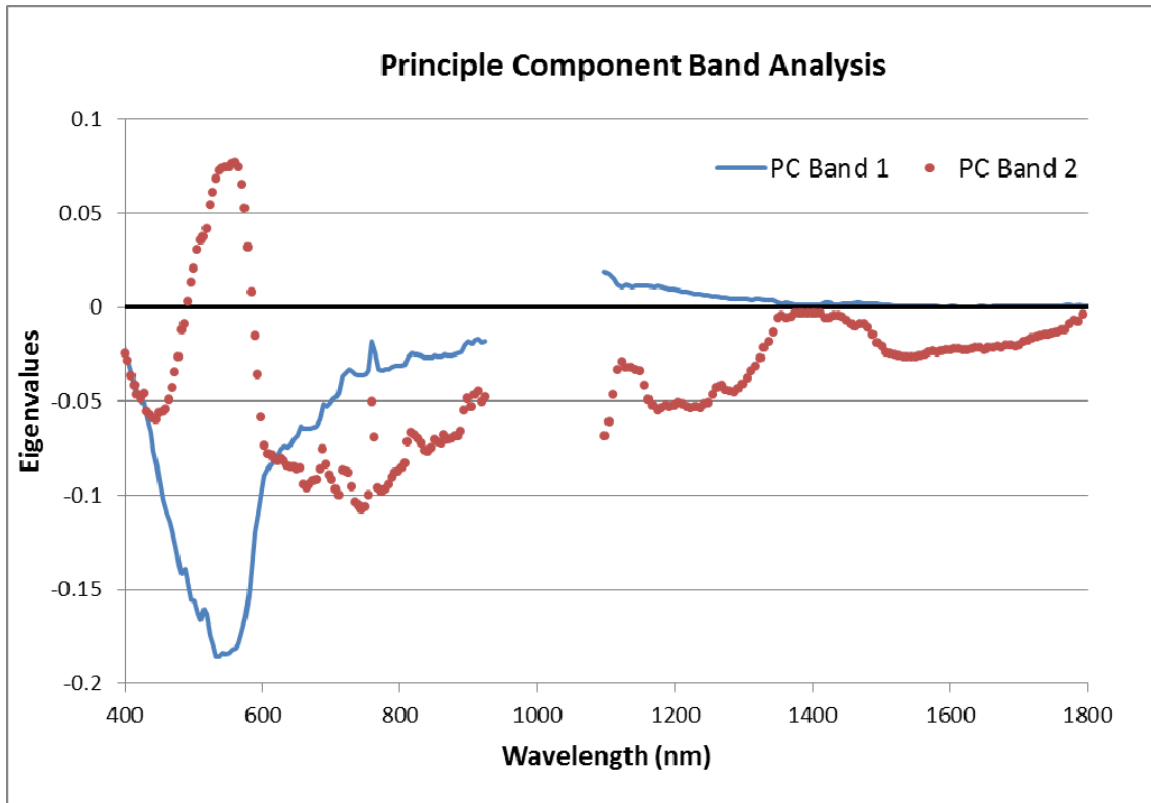
Figure 39.   Plot of line 003 PC eigenvalues. PC band 1 values are the blue line, and PC band 2 values are the red dots. The black line highlights the 0 point as a reference

The positive spike in PC band 2 at about 556 nm indicates that the green wavelengths contribute the most to this band, with negative values for the red, blue and near IR wavelengths. The PC band 1 curve is similar to the spectral irradiance curve shown in Figure 4, but inverted. This is due to the way PC band 1 is calculated: The more intense a pixel, the more negative the score. It shows that PC band 1 contributions are mainly from solar irradiance. Any non-zero values at wavelengths greater than near IR indicate potential target contributions or noise. Future analysis using PC might be more effective if the near IR is isolated from the visual wavelengths first.

VI. CONCLUSIONS

As demonstrated by the economic and military damage caused by the use of naval mines, mine detection capabilities need to outpace the development of increasingly complex mines. While current technologies are reliable, they tend to put operators and assets at risk, or simply have too narrow a field of view to search large areas. If high altitude, hyperspectral imaging can prove a reliable detection mechanism, it would provide the Department of Defense with a safe, wide-area search tool. The promising results of this paper suggest this is a possibility.

A. VISUAL INSPECTION

One of the initial questions one should ask of a hyperspectral dataset meant to detect mines is, "can the targets be visually identified prior to any sort of processing?" Using the ProSpecTIR-VS3 1 meter data, the answer appears to be, "yes." With prior knowledge of where the targets are located, targets are relatively easy to differentiate from the other ocean clutter. The bright colored, reflective targets were, of course the easiest to visually identify. Realistically though, enemy combatants laying mines are not likely to paint their targets bright colors. Regrettably, the limited sample size of dark targets prevented further analysis.

B. ANOMALY DETECTION

Although the targets are visually identifiable in the true-color images, a cueing mechanism is still needed to point the operator to the correct location. In any real-world scenario, there is simply too much water to cover for an operator to examine images pixel by pixel. This study was able to evaluate the feasibility of two different detection algorithms.

1.   RX Anomaly Detector

a.   *Submerged Targets*

Without the ability to un-mix pixels using an input sample target spectrum, the RXD-UTD algorithm was unable to locate the submerged targets effectively. The limited spectral features of the target spectra did not alter the mixed pixel enough to separate it from the background clutter, resulting in 0% submerged target detection. This seems to indicate RX anomaly detection is not a valid solution to this problem.

b.   *Surface Targets*

The RXD-UTD algorithm was able to locate the green and white surface targets, but as discussed earlier, the limitation of RX anomaly detectors is their susceptibility to high false alarm rates. The previously provided example of Bab-el-Mandeb showed the relatively high number of pixels that would be selected incorrectly by the RXD-UTD surface target detection process. As a stand-alone detector, this would be prohibitive, but if used as a cueing mechanism, informing the operator of where to look, this process could increase the speed of detection. Operationally, the user would have to sort through each false pixel (or grouping of pixels) to determine if they are a target or not. Without the anomaly detector, this could be 5.2 million pixels (1 meter spatial resolution, covering an area of 5.2 million meters). This number would be reduced by the RXD-UTD process proposed in this paper.

c.   *Concerns*

(1) Black Target. The success of RXD-UTD in locating the green and white surface targets is muted by the detector's inability to locate the black surface target. As noted earlier, if searching for mines, this is the most realistic color of the targets. The lack of a significant sample size of dark targets prevented further analysis of this particular concern.

(2) Target Isolation. Although target detection wizards exist for the RXD-UTD that are similar to the one used in this paper for MTMF, the RXD-UTD process does not have a logical or scientific way to isolate the target from the background clutter. Even in a wizard the operator must threshold the image at rather arbitrary values until satisfied the targets are isolated. ROC curves can give estimates of false positive and true positive ratios, but in practice, this technique leaves too much room for error and variability.

2. MTMF

a. Submerged Targets

This study has shown the feasibility of using 1 meter hyperspectral data in conjunction with an MTMF target detection wizard in order to detect sub-pixel size mines. With low false positive rates and high true positive rates, the process proposed in the previous chapters appears to be a valid option. As noted in the principle component analysis, the submerged targets appear to have a spectral signature distinct from the surrounding water.

b. Surface Targets

Similar to the RX anomaly detector, the surface MTMF analysis had success in locating the surface targets. With the Mixture-Tuned half of MTMF, the process is able to effectively reduce false alarms, increasing its productivity over other anomaly detectors like the RXD. The principle component analysis showed that, while similar to other surface objects, the surface targets have unique spectral signatures and intensities when compared to the water. Aside from 3 pixels, all of the false alarms were due to non-target surface objects being detected. Operationally, visually distinguishing between false alarms caused by vessels or buoys and true positives is a simple task.

c. Concerns

(1) Black Target. Much like the visual analysis and the RXD-UTD, the MTMF had difficulties locating the black surface target. As shown in the

principle component analysis, this might be due to similarities between the spectral signatures and intensities of the target and water. In this case, the detection of the surface target was also hindered by the presence of the large and highly reflective M/V Merlin. Again, limited sample size prevents further analysis.

(2) Large, Highly Reflective Objects. As shown in the previous example, large, highly reflective objects overpower scatter plots, preventing the isolation of target pixels and increasing the false positive rate. If this is the case, much like the littoral zones and land, the objects would have to be masked out prior to a MTMF analysis.

(3) Input Targets. Operationally, the most limiting factor of a MTMF analysis could be the lack of an input sample target spectrum. This process requires a sample target, spectrally similar to those being searched for, to be imaged at radiometric conditions similar to search area. It is the suggestion of the author that a sample target be placed near the search area and imaged prior to and post surveying of the target area.

C.   FUTURE WORK

A similar test with a more statistically significant number of targets over a larger area would further validate these techniques. Targets closer in shape and color to real mines, placed in a variety of water and weather conditions would also provide an analysis of the usefulness of this technique in real world situations.

Ocean current modeling needs to be done to look at the movement of drifting mines in potential conflict areas. If drifting mines can be found by hyperspectral surveys, their location will have changed by the time an EOD unit can deploy to the area.

Novel work is already done by Leonard and Acker (2012), and Louchard, Farm, and Acker (2008), among others, using multi-look spectral imagers to reduce background clutter. This would decrease false positives in survey conditions similar to those of this test. More importantly, this technology may allow for mine detection in less ideal conditions, including littoral zones, poor weather and high glint situations.

D.   OTHER USES

Although this paper focused on military uses of the detection of sub-pixel objects in hyperspectral images, many other options exist. The MTMF analysis was particularly effective in identifying bright targets, a fact that may prove useful in search and rescue operations. Personal floatation devices tend to contain highly reflective and bright fabrics, an ideal target for MTMF anomaly detection.

THIS PAGE INTENTIONALLY LEFT BLANK

APPENDIX A

Table 9. Original flight plan of survey area for the high resolution collection; the lines that were actually flown are highlighted

Flight line	Flying height (MSL)		Projected WGS84					Ground pixel			Length	Time
	Meters	Feet	line start		line end		Ell. Height	mean	min	max	[nm]	[Min]
1	418	1,371	117° 16' 25.85" W	32° 53' 6.35" N	117° 14' 35.90" W	32° 53' 1.29" N	418	50	55	39	1.6	7
2	417	1,368	117° 16' 27.66" W	32° 53' 3.48" N	117° 14' 34.47" W	32° 52' 58.26" N	417	50	55	39	1.6	7
3	416	1,365	117° 16' 27.98" W	32° 53' 0.57" N	117° 14' 34.53" W	32° 52' 55.34" N	416	50	55	38	1.6	7
4	415	1,362	117° 16' 28.17" W	32° 52' 57.67" N	117° 14' 34.71" W	32° 52' 52.44" N	415	50	54	38	1.6	7
5	414	1,358	117° 16' 28.35" W	32° 52' 54.78" N	117° 14' 34.90" W	32° 52' 49.56" N	414	50	54	38	1.6	7
6	414	1,358	117° 16' 28.54" W	32° 52' 51.90" N	117° 14' 35.09" W	32° 52' 46.67" N	414	50	54	38	1.6	7
7	412	1,352	117° 16' 28.73" W	32° 52' 49.01" N	117° 14' 35.28" W	32° 52' 43.79" N	412	50	54	37	1.6	7
8	410	1,345	117° 16' 28.91" W	32° 52' 46.15" N	117° 14' 35.46" W	32° 52' 40.92" N	410	50	54	37	1.6	7
9	408	1,339	117° 16' 29.09" W	32° 52' 43.30" N	117° 14' 35.65" W	32° 52' 38.07" N	408	50	54	37	1.6	7
10	410	1,345	117° 16' 29.28" W	32° 52' 40.46" N	117° 14' 35.83" W	32° 52' 35.24" N	410	50	54	37	1.6	7
11	411	1,348	117° 16' 29.46" W	32° 52' 37.61" N	117° 14' 36.01" W	32° 52' 32.38" N	411	50	54	38	1.6	7
12	410	1,345	117° 16' 29.65" W	32° 52' 34.76" N	117° 14' 36.20" W	32° 52' 29.53" N	410	50	54	37	1.6	7
13	409	1,342	117° 16' 29.83" W	32° 52' 31.91" N	117° 14' 36.38" W	32° 52' 26.68" N	409	50	54	37	1.6	7
14	409	1,342	117° 16' 30.01" W	32° 52' 29.07" N	117° 14' 36.57" W	32° 52' 23.85" N	409	50	54	37	1.6	7
15	411	1,348	117° 16' 30.19" W	32° 52' 26.24" N	117° 14' 36.75" W	32° 52' 21.01" N	411	50	54	37	1.6	7
16	415	1,362	117° 16' 30.12" W	32° 52' 23.38" N	117° 14' 37.19" W	32° 52' 18.18" N	415	50	54	38	1.6	7
17	418	1,371	117° 16' 28.46" W	32° 52' 20.44" N	117° 14' 39.22" W	32° 52' 15.41" N	418	50	55	38	1.5	7

Table 10.   Original flight plan of survey area for the low resolution collection; all lines were flown

Flight line	Flying height (MSL)		Projected WGS84					Ground pixel			Length	Time
	Meters	Feet	line start		line end		Ell. Height	mean	min	max	[nm]	[Min]
1	803	2,635	117° 16' 27.42" W	32° 53' 4.09" N	117° 14' 34.62" W	32° 52' 58.89" N	803	100	104	88	1.6	5
2	801	2,628	117° 16' 28.18" W	32° 52' 57.40" N	117° 14' 34.73" W	32° 52' 52.17" N	801	100	105	88	1.6	5
3	799	2,622	117° 16' 28.62" W	32° 52' 50.73" N	117° 14' 35.16" W	32° 52' 45.50" N	799	100	104	88	1.6	5
4	796	2,612	117° 16' 29.05" W	32° 52' 44.06" N	117° 14' 35.60" W	32° 52' 38.84" N	796	100	104	87	1.6	5
5	796	2,612	117° 16' 29.47" W	32° 52' 37.43" N	117° 14' 36.03" W	32° 52' 32.21" N	796	100	104	88	1.6	5
6	796	2,612	117° 16' 29.90" W	32° 52' 30.80" N	117° 14' 36.46" W	32° 52' 25.58" N	796	100	104	87	1.6	5
7	799	2,622	117° 16' 30.25" W	32° 52' 24.17" N	117° 14' 36.96" W	32° 52' 18.96" N	799	100	105	88	1.6	5

APPENDIX B

Table 11.   The wavelengths of bands 1 through 180 of the collected ProSpecTIR-VS3 data

Band #	λ (nm)	Band #	λ (nm)	Band #	λ (nm)	Band #	λ (nm)	Band #	λ (nm)	Band #	λ (nm)
1	391	31	528	61	669	91	812	121	966	151	1156
2	396	32	533	62	674	92	817	122	972	152	1162
3	400	33	538	63	679	93	822	123	978	153	1168
4	405	34	542	64	683	94	827	124	985	154	1175
5	409	35	547	65	688	95	831	125	991	155	1181
6	414	36	552	66	693	96	836	126	997	156	1187
7	419	37	556	67	698	97	841	127	1003	157	1193
8	423	38	561	68	702	98	846	128	1009	158	1199
9	428	39	566	69	707	99	851	129	1016	159	1205
10	432	40	570	70	711	100	855	130	1022	160	1211
11	437	41	575	71	716	101	860	131	1029	161	1218
12	442	42	580	72	721	102	865	132	1035	162	1224
13	446	43	585	73	726	103	870	133	1042	163	1230
14	451	44	589	74	731	104	875	134	1048	164	1236
15	455	45	594	75	735	105	880	135	1055	165	1243
16	460	46	598	76	740	106	884	136	1061	166	1249
17	465	47	603	77	745	107	889	137	1067	167	1255
18	469	48	608	78	750	108	894	138	1073	168	1261
19	474	49	613	79	754	109	899	139	1080	169	1268
20	478	50	618	80	759	110	904	140	1086	170	1274
21	483	51	622	81	764	111	909	141	1092	171	1280
22	487	52	627	82	769	112	914	142	1098	172	1286
23	492	53	632	83	774	113	919	143	1104	173	1293
24	497	54	636	84	778	114	924	144	1110	174	1299
25	501	55	641	85	783	115	929	145	1117	175	1305
26	506	56	646	86	788	116	934	146	1123	176	1311
27	510	57	650	87	793	117	939	147	1130	177	1318
28	515	58	655	88	798	118	946	148	1136	178	1324
29	519	59	660	89	803	119	952	149	1143	179	1331
30	524	60	665	90	807	120	959	150	1149	180	1337

Table 12.   The wavelengths of bands 181 through 360 of the collected ProSpecTIR-VS3 data

Band #	λ (nm)	Band #	λ (nm)	Band #	λ (nm)	Band #	λ (nm)	Band #	λ (nm)	Band #	λ (nm)
181	1343	211	1532	241	1720	271	1909	301	2095	331	2282
182	1350	212	1538	242	1726	272	1915	302	2101	332	2288
183	1356	213	1544	243	1732	273	1921	303	2107	333	2294
184	1362	214	1551	244	1738	274	1927	304	2113	334	2300
185	1369	215	1557	245	1744	275	1933	305	2120	335	2306
186	1375	216	1563	246	1750	276	1939	306	2126	336	2313
187	1381	217	1569	247	1756	277	1945	307	2132	337	2319
188	1387	218	1576	248	1762	278	1951	308	2139	338	2325
189	1393	219	1582	249	1768	279	1957	309	2145	339	2331
190	1400	220	1588	250	1775	280	1964	310	2151	340	2337
191	1406	221	1594	251	1781	281	1970	311	2157	341	2344
192	1412	222	1601	252	1787	282	1976	312	2164	342	2350
193	1418	223	1607	253	1794	283	1982	313	2170	343	2356
194	1425	224	1613	254	1800	284	1988	314	2176	344	2362
195	1431	225	1619	255	1806	285	1994	315	2182	345	2369
196	1437	226	1625	256	1813	286	2001	316	2188	346	2376
197	1444	227	1632	257	1819	287	2007	317	2194	347	2383
198	1450	228	1638	258	1826	288	2013	318	2200	348	2389
199	1456	229	1644	259	1832	289	2019	319	2206	349	2396
200	1463	230	1650	260	1838	290	2026	320	2213	350	2403
201	1469	231	1657	261	1845	291	2032	321	2219	351	2409
202	1475	232	1663	262	1851	292	2038	322	2225	352	2415
203	1482	233	1669	263	1857	293	2044	323	2232	353	2422
204	1488	234	1676	264	1864	294	2051	324	2238	354	2428
205	1495	235	1682	265	1870	295	2057	325	2244	355	2434
206	1501	236	1689	266	1876	296	2063	326	2251	356	2440
207	1507	237	1695	267	1883	297	2070	327	2257	357	2446
208	1514	238	1701	268	1889	298	2076	328	2263	358	2453
209	1520	239	1708	269	1896	299	2082	329	2269	359	2459
210	1526	240	1714	270	1902	300	2088	330	2276	360	2465

84

LIST OF REFERENCES

Acker, A., Pfeiffer, J. E., & Farm, B. (2003). Automated sub-pixel target detection using the LASH hyperspectral sensor. In *Proceedings of SPIE, vol. 5093* (pp. 731–739). Orlando, FL, USA.

Ashton, E.A. & Schaum, A. (1998). Algorithms for the detection of sub-pixel targets in multispectral imagery. *Photogrammetric Engineering & Remote Sensing, July 1998* (pp. 723-731).

Banerjee, A., Burlina, P. & Diehl, C. (2006). A support vector method for anomaly detection in hyperspectral imagery. *Geoscience and Remote Sensing, IEEE Transactions on.* 44(8), 2282–2291.

Barnes, C., Gilbert, G., Schoonmaker, J., & Rohr, J. (1999). The possibility of passive whale tracking with the use of a hyperspectral sensor. In *OCEANS '99 MTS/IEEE. Riding the Crest into the 21st Century, vol.1* (pp. 141–144). Seattle, WA, USA.

Barrow, B., & Nelson, H. H. (2001). Model-based characterization of electromagnetic induction signatures obtained with the MTADS electromagnetic array. *Geoscience and Remote Sensing, IEEE Transactions on.* 39(6), 1279–1285.

Blankenship, J. R. (2006). *Assessing the Ability of Hyperspectral Data to Detect Lyngbya SPP.: A Potential Biological Indicator for Presence of Metal Objects in the Littoral Environment* (Master's Thesis, Naval Postgraduate School). Retrieved from http://www.dtic.ml

Boardman, J. W. (1993). Automated spectral unmixing of AVIRIS data using convex geometry concepts. *Summaries of the Fourth JPL Airborne Geoscience Workshop* (pp.53–56). 93–26, Pasadena, CA, USA: JPL Publications.

Boardman, J. W. (1998). Leveraging the high dimensionality of AVIRIS data for improved sub-pixel target unmixing and rejection of false positive: Mixture tuned match filtering. In. R. O. Green (Eds.), *Summaries of the Seventh JPL Airborne Geoscience Workshop* (pp. 55). Pasadena, CA, USA: JPL Publications.

Boardman, J. W. & Kruse, F. A. (2011). Analysis of imaging spectrometer data using - dimensional geometry and a mixture-tuned matched filtering approach. *Geoscience and Remote Sensing, IEEE Transactions on, 49*(11), 4138–4152.

Borden, S. A. (2000). *Mine countermeasures: A comparative analysis of US Navy mine countermeasures 1999 vs. 2020* (Strategy Research Report No. ADA377403). Carlisle Barracks, PA: U.S. Army War College.

Brown, D. K. (1990). Before the ironclad: Development of ship design, propulsion, and armament in the Royal Navy, 1815–60. London: Naval Institute Press.

Bukata, R. P. (1995). *Optical properties and remote sensing of inland and coastal waters*. Boca Raton, Fla.: CRC Press.

Butler, A. (2011, Sept. 19). USAF turns to hyperspectral sensors in Afghanistan. *Aviation Week & Space Technology*. Retrieved from http://www.aviationweek.com

Chang, C. I. & Chiang, S. S. (2002). Anomaly detection and classification for hyperspectral imagery. *Geoscience and Remote Sensing, IEEE Transactions on, 40*(6), 1314–1325.

Clark, R. N. (1999). Spectroscopy of rocks and minerals, and principles of spectroscopy. In A. N. Rencz (Eds.), *Manual of remote sensing, volume 3: Remote sensing for the earth science* (pp. 3-58). New York, NY: John Wiley and Sons.

Cox, C., & Munk, W. (1954). Measurement of the roughness of the sea surface from photographs of the sun's glitter. *J.Opt.Soc.Am., 44*(11), 838–850.

DiPietro, R. S. (2010). *The detection of sub-pixel objects and mitigation of false alarms in hyperspectral imagery* (Master's thesis, Northeastern University). Retrieved from http://iris.lib.neu.edu

DiPietro, R. S., Manolakis, D., Lockwood, R., Cooley, T., & Jacobson, J. (2010). Performance evaluation of hyperspectral detection algorithms for subpixel objects. In *Proceedings of SPIE, Vol. 7695, Algorithms and Technologies for Multispectral, Hyperspectral, and Ultraspectral Imagery XVI* (pp. 76951W1–76951W11).

Doxaran, D., Froidefond, J. M., Lavender, S. & Castaing, P. (2002). Spectral signature of highly turbid waters: Application with SPOT data to quantify suspended particulate matter concentrations. *Remote Sensing of Environment.* 81(1), 149–161.

ENVI Help, Version 4.8. Normalized Vegetation Difference Index. Accessed Feb. 2012.

Funk, R. L., Feldpausch, R. J., & Bridge, B. (2011). *Wide area assessment (WAA) for marine munitions and explosives of concern* (ESTCP Report No. MR-200808).

Gilbert, J. A. (2001). *The combined mine countermeasures force: a unified commander-in-chief's answer to the mine threat* (Report No. AD-A186). Newport, R.I.: Naval War College, Joint Military Operations Department.

Goetz, A. F. H., Vane, G., Solomon, J. E., & Rock, B. N. (1985). Imaging spectrometry for earth remote sensing. *Science, 228*(4704), 1147–1153.

Goetz, A. F. H. (1992). Principles of narrow band spectrometry in the visible and IR: instruments and data analysis. In: F. Toselli and J. Bodechtel (Eds.), *Imaging Spectroscopy: Fundamentals and Prospective Applications* (pp. 21–32). Dordrecht, The Netherlands: Kluwer Academic Publishers.

Goetz, A. F. H. & Curtiss, B. (1996). Hyperspectral imaging of the Earth: Remote analytical chemistry in an uncontrolled environment. *Field Analytical Chemistry & Technology*. 1(2), 67–76.

Goetz, A. F. H, Boardman, J. W., Kindel, B. C., & Heidebrecht, K. B. (1997). Atmospheric corrections: on deriving surface reflectance from hyperspectral imagers. In *Proceedings of SPIE Vol. 3118, Imaging Spectrometry III* (pp. 14–22). San Diego, CA, USA.

Goodrich ISR Systems (2012, March). *La Jolla Collection Test Plan, Version 9* (Unpublished Internal Report). Author.

Green, A. A., Berman, M., Switzer, P., & Craig, M. D. (1988). A transformation for ordering multispectral data in terms of image quality with implications for noise removal. *Geoscience and Remote Sensing, IEEE Transactions on, 26*(1), 65–74.

Green, R. O., Eastwood, M. L., Sarture, C. M., Chrien, T. G., Aronsson, M., Chippendale, B. J., et al. (1998). Imaging spectroscopy and the airborne visible/infrared imaging spectrometer (AVIRIS). *Remote Sensing of Environment, 65*(3), 227–248.

Harsanyi, J. C., Farrand, W. H. & Chang, C. I. (1994). Detection and classification of subpixel signatures in hyperspectral image sequences. In *Proceedings of American Society for Photogrammetry and Remote Sensing (pp. 236–247).* Reno, NV, USA.

Hayes, M. P. & Gough, P. T. (1999). Using synthetic aperture sonar for mine detection, In *Proceedings of Australian-American Joint Conference on the Technology of Mines and Mine Countermeasure Systems* (pp.1.1–1.10). Sydney, Australia.

Healey, G., & Slater, D. (1999). Models and methods for automated material identification in hyperspectral imagery acquired under unknown illumination and atmospheric conditions. In *Geoscience and Remote Sensing, IEEE Transactions on, 37*(6), 2706–2717.

Hedley, J. D., Harborne, A. R., & Mumby, P. J. (2005). Simple and robust removal of sun glint for mapping shallow-water benthos. *International Journal of Remote Sensing, 26*(10), 2107–2112.

Hochberg, E. J., Andrefouet, S., & Tyler, M. R. (2003). Sea surface correction of high spatial resolution Ikonos images to improve bottom mapping in near-shore environments. *Geoscience and Remote Sensing, IEEE Transactions on, 41*(7), 1724–1729.

Hochberg, E. J., Mobley, C. D., Park, Y., Goodman, J., Turpie, K. R., Gao, B., et al. (2011). HyspIRI sunglint subgroup: Glint characterization, determination of impacts on science, and potential mitigation approaches [Presented Slides]. Paper presented at 2011 HyspIRI Science Workshop - NASA Decadal Survey Mission. Washington, DC.

Jensen, J. R. (2005). *Introductory digital image processing: a remote sensing perspective* (3rd ed.). Upper Saddle River, N.J.: Prentice Hall.

Jensen, J. R. (2008). *Remote sensing of the environment: an Earth resource perspective* (2nd ed.). Upper Saddle River, N.J.: Prentice Hall.

Kay, S., Hedley, J. D., & Lavender, S. (2009). Sun glint correction of high and low spatial resolution images of aquatic scenes: A review of methods for visible and near-infrared wavelengths. *Remote Sensing, 1*(4), 697–730.

Kruse, F. A. (1999). Visible-infrared sensors and case studies. In S.A. Morain and A.M. Budge (Eds.), *Manual of Remote Sensing* (Chapter 11), 3rd Ed. Falls Church, VA: American Society for Photogrammetry and Remote Sensing.

Kruse, F. A. (2003, February). *Mineral mapping with AVIRIS and EO-1 Hyperion.* Paper presented at the 12th JPL Airborne Geoscience Workshop, Pasadena, CA, USA.

Kruse, F. A., Boardman, J. W. & Huntington, J. F. (2003). Comparison of airborne hyperspectral data and EO-1 Hyperion for mineral mapping. *Geoscience and Remote Sensing, IEEE Transactions on, 41*(6), 1388–1400.

Kutser, T., Vahtmäe, E., & Praks, J. (2009). A sun glint correction method for hyperspectral imagery containing areas with non-negligible water leaving NIR signal. *Remote Sensing of Environment, 113*(10), 2267–2274.

Kwon, H. & Nasrabadi, N. M. (2005). Kernel RX-algorithm: A nonlinear anomaly detector for hyperspectral imagery. *Geoscience and Remote Sensing, IEEE Transactions on, 43*(2), 388–397.

Leonard, C. L., Chan, C. W., Cottis, T., DeWeert, M., Dichner, M., Farm, B., et al. (2008). TACMSI: A novel multi-look multispectral imager for maritime mine detection. In *Proceedings of SPIE, Vol. 6953, Detection and Sensing of Mines, Explosive Objects and Obscured Targets XIII* (pp. 69530N:1–5). Orlando, FL, USA.

Lillesand, T. M., & Kiefer, R. W. (2000). *Remote sensing and image interpretation* (4th ed.). New York: John Wiley & Sons.

Louchard, E., Farm, B., & Acker, A. (2008). Performance analysis of a multispectral framing camera for detecting mines in the littoral zone and beach zone. In *Proceedings of SPIE, Vol. 6946, Airborne Intelligence, Surveillance, Reconnaissance (ISR) Systems and Applications V* (pp. 694609:1–11). Orlando, FL, USA.

Malinici, I. P. (2004). *Active learning and transductive inference for detection of concealed targets* (Master's Thesis, Duke University). Retrieved from http://www.genome.duke.edu

Mars, J. C., & Crowley, J. K. (2003). Mapping mine wastes and analyzing areas affected by selenium-rich water runoff in southeast Idaho using AVIRIS imagery and digital elevation data. *Remote Sensing of Environment, 84*(3), 422–436.

Miao, X., Azimi-Sadjadi, M. R., Bin Tan, Dubey, A. C., & Witherspoon, N. H. (1998). Detection of mines and minelike targets using principal component and neural-network methods. *Neural Networks, IEEE Transactions on, 9*(3), 454–463.

Microimages, Inc. (2001). *Introduction to hyperspectral imaging with TNTmips*. Lincoln, NE, USA: Author

Mobley, C. D. (1994). *Light and water: Radiative transfer in natural waters*. San Diego: Academic Press.

Muise, R. R., Wright, J. A, Holmes, Q. A. (1996). Coastal mine detection using the COBRA multispectral sensor. In *Proceedings of SPIE, Vol. 2765, Detection and Remediation Technologies for Mines and Minelike Targets* (pp. 15–24). Orlando, FL, USA.

Mustard, J. F., Staid, M. I., & Fripp, W. J. (2001). A semianalytical approach to the calibration of AVIRIS data to reflectance over water application in a temperate estuary. *Remote Sensing of Environment, (75), 335–349.

Nash, D. B., and Conel, J. E. (1974), Spectral reflectance systematics for mixtures of powdered Hypersthene, Labradorite, and Ilmenite, *Journal of Geophysical Research*, 79(11), 1615–1621.

Needham, J., & Wang, L. (1954). *Science and civilisation in China, Volume 5, Part 7.* Cambridge University Press.

Olsen, R. C. (2007). *Remote sensing from air and space*. Bellingham, Wash.: SPIE Press.

Potter, J. (1999). Challenges of seeing underwater -a vision for tomorrow. Paper presented at the *Naval Platform Technology Seminar,* Singapore.

Program Executive Office Littoral and Mine Warfare (PEO LMW). (2009). *21st century US navy mine warfare: Ensuring global access and commerce* (US Navy Expeditionary Warfare Directorate Report). Washington, DC.: US Navy PEO LMW.

Reed, I. S., & Yu, X. (1990). Adaptive multiple-band CFAR detection of an optical pattern with unknown spectral distribution. *Acoustics, Speech and Signal Processing, IEEE Transactions on, 38*(10), 1760–1770.

Rios, J. J. (2005, July) *Naval mines in the 21st century: Can NATO navies meet the challenge* (Master's thesis, Naval Postgraduate School). Retrieved from https://www.dtic.mil

Sandersfeld, M. (2012). *Detection of subpixel submerged mine-like targets in Worldview-2 multispectral imagery.* (Master's Thesis, Naval Postgraduate School).

Schweizer, S. M., & Moura, J. M. F. (2000). Hyperspectral imagery: Clutter adaptation in anomaly detection. *Information Theory, IEEE Transactions on, 46*(5), 1855–1871.

Shippert, P. (2003). Introduction to hyperspectral image analysis. *Online Journal of Space Communication,* (3) Retrieved from https:// spacejournal.ohio.edu/

Silva, D. M., & Abileah, R. (1998). Two algorithms for removing ocean surface clutter in multispectral and hyperspectral images. Paper presented at *Ocean Optics XIV,* Kailua-Kona, Hawaii.

Singer, R. B., & McCord, T. B. (1979) Mars - Large scale mixing of bright and dark surface materials and implications for analysis of spectral reflectance. In *Proceedings of 10th Lunar and Planetary Science Conference, Vol. 2* (pp.1835–1848). Houston, TX, USA.

SpecTIR, LLC. (2011). *SpecTIR ProSpecTIR VS* (Product Brochure). Reno, NV: Author.

SpecTIR, LLC. (2012). *SRS project report: Goodrich, La Jolla, California* (Report No. 1530). Reno, NV: Author.

Stein, D., Schoonmaker, J., & Coolbaugh, E. (2001). *Hyperspectral imaging for intelligence, surveillance, and reconnaissance* (Research Paper No. A421434). San Diego, CA: Space and Naval Warfare Systems Center.

Stein, D. W., Beaven, S. G., Hoff, L. E., Winter, E. M., Schaum, A. P., & Stocker, A. D. (2002). Anomaly detection from hyperspectral imagery. *Signal Processing Magazine, IEEE, 19*(1), 58-69.

Stocker, A. D., & Schaum, A. P. (1997). Application of stochastic mixing models to hyperspectral detection problems. In *Proceedings of SPIE, Vol. 3071, Algorithms for Multispectral and Hyperspectral Imagery III* (pp. 47–60). Orlando, FL, USA.

Truver, S. C. (2011). Taking mines seriously: Mine warfare in China's near seas. *Naval War College Review, 65*(2), 30–66.

Vahtmae, E., & Kutser, T. (2008). Sun glint correction of airborne AISA images for mapping shallow-water benthos. In *US/EU-Baltic International Symposium, 2008 IEEE/OES* (pp. 1–8). Tallinn, Estonia.

van der Meer, F., & de Jong, S. M. (2002). *Imaging spectrometry: Basic principles and prospective applications*. Dordrecht ; Boston: Kluwer Academic Publishers.

Vane, G., & Goetz, A. F. H. (1988). Terrestrial imaging spectroscopy. *Remote Sensing of Environment, 24*(1), 1–29.

von Alt, C., Allen, B., Austin, T., Forrester, N., Goldsborough, R., Purcell, M., et al. (2001). Hunting for mines with REMUS: A high performance, affordable, free swimming underwater robot. In *OCEANS, 2001. MTS/IEEE Conference and Exhibition, Vol. 1.* (pp. 117–122). Honolulu, HI, USA.

Williams, D. P., Myers, V., & Silvious, M. S. (2009). Mine classification with imbalanced data. *Geoscience and Remote Sensing Letters, IEEE, 6*(3), 528–532.

Witherspoon, N. H., Hollway Jr., J. H., Davis, K. S., Miller, R. W. & Dubey, A. C. (1995) The coastal battlefield reconnaissance and analysis (COBRA) program for minefield detection. In *Proceedings of SPIE, Vol. 2496, Detection Technologies for Mines and Minelike Targets* (pp. 500–508). Orlando, FL, USA.

Winter, E. M., & Silvious, M. S. (2008). Spectral methods to detect surface mines. In *Proceedings of SPIE, Vol. 6953, Detection and Sensing of Mines, Explosive Objects and Obscured Targets XIII* (pp.69530R:1–9). Orlando, FL, USA.

Yu, X., Reed, I. S. & Stocker, A. D. (1993). Comparative performance analysis of adaptive multispectral detectors. *Signal Processing, IEEE Transactions on, 41*(8), 2639–2656.

Yu, X., Hoff, L.E., Reed, I. S., Chen, A. M. & Stotts, L. B. (1997). Automatic target detection and recognition in multiband imagery: A unified ML detection and estimation approach. *Image Processing, IEEE Transactions on, 6*(1), 143–156.

THIS PAGE INTENTIONALLY LEFT BLANK

INITIAL DISTRIBUTION LIST

1.   Defense Technical Information Center
        Ft. Belvoir, Virginia

2.   Dudley Knox Library
        Naval Postgraduate School
        Monterey, California

3.   Dr. Richard C. Olsen
        Remote Sensing Center, Naval Postgraduate School
        Monterey, California
        olsen@nps.edu

4.   Col. (Ret.) David Trask
        Naval Postgraduate School
        Monterey, California
        dmtrask@nps.edu

5.   Maj. Neal Hinson
        Headquarters Air Force A2
        Washington, D.C.
        neal.hinson@pentagon.af.mil

6.   Maj. Joshua Smith
        Beale Air Force Base
        Beale Air Force Base, California
        joshua.smith@beale.af.mil

7.   Kevin Whitcomb
        UTC Aerospace Systems
        Westford, MA
        kevin.whitcomb@utas.utc.com

8.   Dr. Dan C. Boger
        Naval Postgraduate School
        Monterey, California
        dboger@nps.edu